Research Square

Preprints are preliminary reports that have not undergone peer review.
They should not be considered conclusive, used to inform clinical practice,
or referenced by the media as validated information.

Bandgap-adjusted bismuth tungstate-titanium dioxide S-scheme heterojunctions: Optimizing interfacial electronic structure for rapid VOC mineralization

Qian Yin
Hanyang University
Hubdar Ali Maitlo
Hanyang University
Ki-Hyun Kim
kkim61@hanyang.ac.kr

Hanyang University

Research Article

Keywords: Formaldehyde, Photocatalytic air purification, TiO2-Bi2WO6 S-scheme, Charge transfer and reaction mechanism

Posted Date: April 30th, 2026

DOI: https://doi.org/10.21203/rs.3.rs-9277031/v1

License: This work is licensed under a Creative Commons Attribution 4.0 International License.
Read Full License

Additional Declarations: No competing interests reported.

Version of Record: A version of this preprint was published at Advanced Composites and Hybrid Materials on June 18th, 2026. See the published version at https://doi.org/10.1007/s42114-026-01932-2.

Bandgap-adjusted bismuth tungstate-titanium dioxide S-scheme heterojunctions: Optimizing interfacial electronic structure for rapid VOC mineralization

Qian Yin [a], Hubdar Ali Maitlo [a], Ki-Hyun Kim [a, *]

[a] Department of Civil and Environmental Engineering, Hanyang University, 222 Wangsimni-Ro, Seoul 04763, Republic of Korea

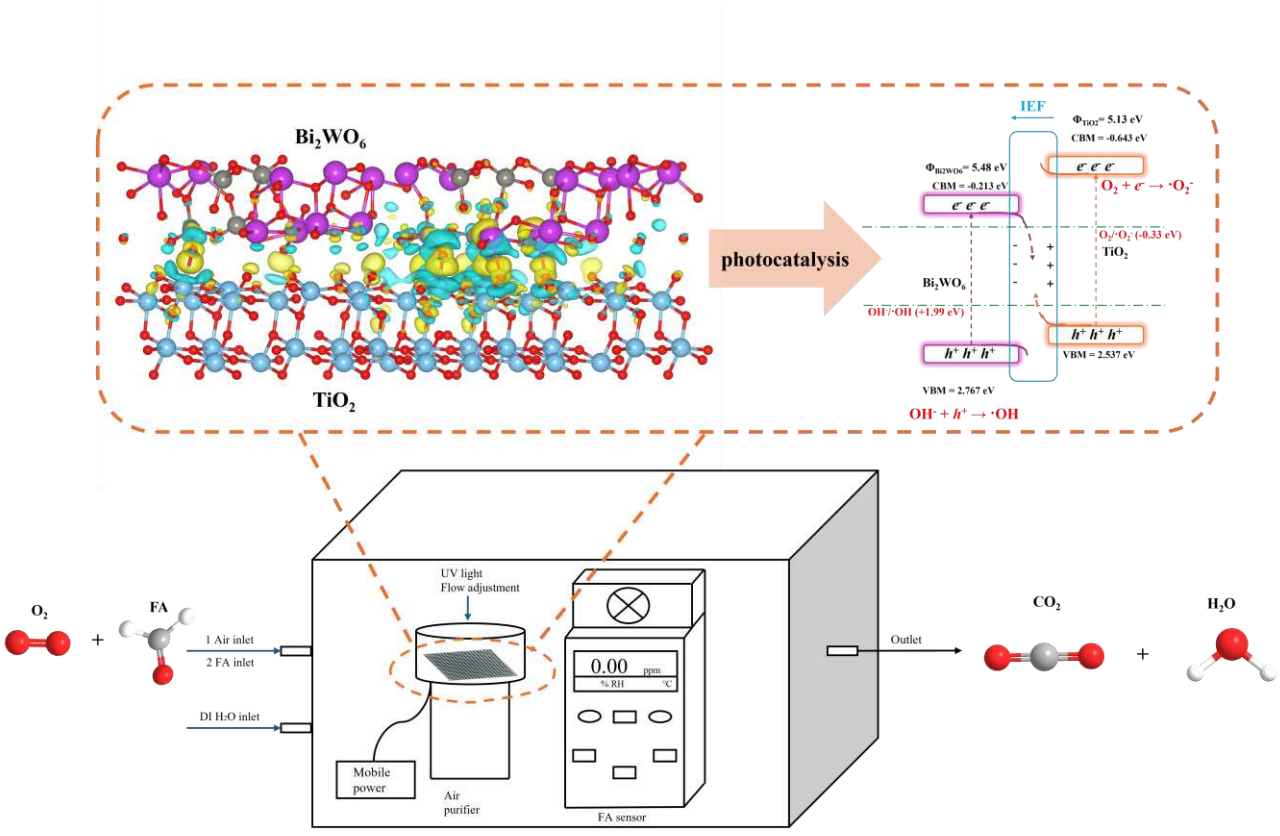
Abstract

To strategically overcome the shortcomings of conventional photocatalysts, particularly inadequate redox potentials, a series of precisely engineered TiO_2-Bi_2WO_6 heterojunction photocatalysts, coded as TB-x (x presents the molar ratio% of Bi:Ti), has been designed through deliberate bandgap adjustment. An optimal interfacial electronic structure, formed by coupling wide-bandgap TiO_2 (3.0–3.2 eV) with narrower-bandgap Bi_2WO_6 (2.6–2.9 eV), enables efficient charge dynamics under low-intensity UV irradiation (~1 W). The optimized TB-5 demonstrates complete removal of 5 ppm formaldehyde (FA: 100% X_{FA}) within 600 seconds, achieving a clean air delivery rate of 10.37 L min^{-1} and apparent quantum yield of 2.68E-01%. The exceptional activity is supported by the formation of a robust S-scheme heterojunction, as confirmed both experimentally and theoretically via density functional theory calculations. This charge preservation mechanism demonstrates remarkable robustness, achieving an 81.6% conversion of FA to CO_2 in 2 hours even at a FA concentration of 100 ppm. *In-situ* DRIFTS analysis further suggests that FA oxidation proceeds sequentially through dioxymethylene and formate intermediates. This work thus establishes a foundational strategy for practical indoor air purification by integrating advanced S-scheme design with atomic-level mechanistic insight, charting a clear path from lab-scale discovery to real-world application

Keywords: Formaldehyde; Photocatalytic air purification; TiO_2-Bi_2WO_6 S-scheme; Charge transfer and reaction mechanism

***Correspondence:** kkim61@hanyang.ac.kr **(K.-H. Kim)**

Graphical abstract



1. Introduction

Formaldehyde (FA), a colorless gas at room temperature, is one of the most persisting indoor air pollutants [1,2]. The high level of indoor FA concentration is typically associated with diverse sources such as cooking, smoking, building materials, and furniture [3-5]. Due to the widespread presence and significant adverse effects on human health, FA has often been taken as a priority target for indoor air pollution control. Given its harmful health impacts, the World Health Organization (WHO) has set a short-term (30-minute) exposure limit of 0.1 mg m^{-3} (0.08 ppm) for indoor FA in 2010 [6]. Therefore, controlling FA levels in indoor air is essential for maintaining good air quality and safeguarding human health.

In recent years, photocatalytic degradation (PCD) technology has been widely applied for the treatment of gaseous pollutants due to its high efficiency, safety, stability, and low energy consumption. Photocatalysts can utilize light energy to decompose gaseous FA into harmless products such as water (H_2O) and carbon dioxide (CO_2) under ambient conditions [7]. TiO_2 is considered one of the most promising photocatalytic semiconductor materials due to its non-toxicity, low cost, and high stability [8]. However, fast recombination of photogenerated charge carriers and weak light absorption limit its application in photocatalytic systems [9]. To address these limitations, diverse modification strategies have been proposed and explored, including TiO_2 doping with noble/transition metals/non-metals and the formation of heterojunctions (e.g., type I, type II, p-n, Z-scheme, and S-scheme). Many of these approaches have been demonstrated as effective options to upgrade the photocatalytic performance of TiO_2-based catalytic materials [10,11]. Among these, the S-scheme heterojunction stands out as a superior strategy, engineered to boost photocatalytic performance through a directed charge transfer pathway that simultaneously maximizes charge separation and preserves high redox potentials [12]. By optimizing the band structure

and enhancing the light absorption capacity, the S-scheme heterojunction materials overcome the limitations of traditional photocatalysts (such as TiO_2) in carrier recombination and weak light absorption [13]. They could also demonstrate excellent FA removal efficiency in practical applications. [14]. In addition, S-scheme heterojunction materials show high stability and high efficiency under a variety of experimental conditions, standing out as a feasible and promising option for removing indoor FA [15].

The utility of bismuth-based compounds, in a range of photocatalytic applications, from the oxidation of indoor organic air pollutants to CO_2 conversion and H_2 production is well known and stems from their unique layered structure, high chemical stability, and strong optical properties [16,17]. Bi_2WO_6, a typical and simple Aurivillius oxide, possesses an orthorhombic structure composed of $[Bi_2O_2]^{2+}$ layers interconnected by $[WO_4]^{2-}$ layers [18]. This structure arrangement is an advantageous feature for the separation of photogenerated electron-hole pairs at coordinatively unsatured surface sites. In addition, Bi_2WO_6 has a lower bandgap (i.e., 2.6-2.9 eV) because of higher valence band (VB) and lower conduction band (CB) made of Bi 6s/O 2p orbitals and W 5d orbitals, respectively [19]. It enables visible-light response while retaining sufficient oxidation ability for reactive oxygen species (ROS) generation. These physicochemical features render Bi_2WO_6 particularly suitable for gas-phase FA oxidation enabling rapid oxygen activation, efficient use of surface hydroxyl species, and sustained oxidation of oxygenated intermediates. Therefore, forming an S-scheme heterojunction by coupling visible light-responsive Bi_2WO_6 with wide-bandgap TiO_2 (3.0-3.2 eV) is a proven strategy for enhancing photocatalytic performance. Over the past few decades, TiO_2-Bi_2WO_6 (TB) systems have been deployed for diverse applications, including wastewater remediation [20-22], photoelectric chemical conversion [23,24], CO_2 methanation reaction [25,17], and antibacterial application [26,27]. Despite this diverse

utility, its performance in simulated indoor environments has scarcely been explored.

To fill this research gap, this study systematically uncovers the fundamental mechanisms of gas-phase FA oxidation over TB-x composites. Although the feasibility of TB-x heterojunctions has been explored for aqueous applications, their operation in gas-phase environments has poorly been investigated. Unlike aqueous systems, gas-phase photocatalysis is hindered by limited reactant adsorption, reduced surface residence times, and the lack of a bulk solvent for continuous hydroxyl precursor supply. Furthermore, these systems exhibit high sensitivity to relative humidity and the inhibitory accumulation of intermediates. Consequently, maximizing interfacial charge separation while preserving high redox potentials is more critical in gas-phase operations than in their liquid-phase counterparts [28,29]. The study presents two key advances: first, the definitive proof of a high-performance S-scheme charge transfer mechanism is established, distinguishing it from conventional Type-II pathways. Second, the surface reaction pathway and key intermediates are elucidated in real-time. By integrating practical performance evaluation with advanced characterization tools, including UPS, XPS, EIS, and in-situ diffuse reflectance infrared Fourier transform spectroscopy (DRIFTS), coupled with theoretical density functional theory (DFT) simulations, we provide unequivocal evidence for the S-scheme pathway and track the mineralization process of FA.

Although TiO_2-Bi_2WO_6 heterojunctions are well known for their effectiveness in treating contaminated water, how they perform and function in the much more demanding gas phase is still poorly understood. Unlike in liquid systems, gas-phase photocatalysis faces major limitations, such as weaker adsorption of reactants, shorter time that molecules stay on the catalyst surface, and the lack of a liquid solvent to supply hydroxyl groups needed for

reactions.

To address these issues, this study carefully designs a series of TB-x heterojunctions by adjusting their bandgap alignment to create a robust S-scheme charge transfer structure. The novelty of this work lies in two key aspects. First, instead of relying solely on observations, we provide clear experimental and theoretical (DFT) evidence for the S-scheme pathway. We demonstrate how it preserves strong redox potentials that enable rapid oxygen activation even under low-intensity light. Second, we use in-situ DRIFTS to create a real-time, molecular-level map of the formaldehyde breakdown process, identifying the key step where dioxymethylene transforms into formate intermediates. By connecting atomic-scale electronic tuning to practical performance metrics such as Clean Air Delivery Rate (CADR), this study establishes a foundational framework for designing high-performance, scalable S-scheme catalysts for sustainable indoor air purification.

2. Experiment

2.1 Materials and chemicals

AEROXIDE® TiO_2 P25 was procured from Evonik Industries AG (Essen, Germany). $Bi(NO_3)_3 \cdot 5H_2O$ (98%), $Na_2WO_4 \cdot 2H_2O$ (≥99%), and paraformaldehyde (pFA (95%)) were purchased from Sigma-Aldrich (St. Louis, Missouri, United States of America (USA)). Ethylene glycol (EG) was purchased from Daejung chemicals & metals Co., Ltd (Siheung, South Korea). Nitrogen (N_2 (99.999%)) and air (99.999%) cylinders were purchased from Union Gas Co., Ltd. (Yongin, South Korea). The FA gaseous primary standard (G-PS) was prepared by thermally decomposing pFA at 110°C under an N_2 flow. The FA G-PS was stored in a polyester aluminum (PEA) bag. Honeycomb ceramic (HC) filters (55 x 55 x 10 cm (2 mm hole size)) were supplied by Pingxiang Zhongci Environmental Ceramics

Material Co., Ltd. (Pingxiang, China).

2.2 Photocatalyst synthesis

The preparation of TiO_2-Bi_2WO_6 (TB-x) samples has been done by modifying the procedures reported previously [20]. Different quantities of $Bi(NO_3)_3 \cdot 5H_2O$ and $Na_2WO_4 \cdot 2H_2O$ were added to a 50 mL glass beaker containing 40 mL EG, to ensure the molar ratio of $Bi(NO_3)_3 \cdot 5H_2O$ and $Na_2WO_4 \cdot 2H_2O$ in 2:1 ratio *(Table S1)*. The solution was stirred for 5 min under ambient conditions. After that, 1 g TiO_2 was added to the above mixture solution and stirred continuously under ambient conditions for 180 min. The resultant suspension was then transferred to a stainless-steel autoclave and hydrothermally treated at 160°C for 15 h. After cooling down to room temperature, the sample was centrifuged to collect the light-yellow slurry. This light-yellow slurry was washed with deionized (DI) water 3 times and then placed in a convection oven operated at 85°C for 12 h to obtain the dry solid powder. The obtained dry powder was labeled x% TiO_2-Bi_2WO_6 (TB-x; where x denotes the molar ratio of Bi to Ti). The preparation of the Bi_2WO_6 follows a procedure analogous to that used for TB-x, with the distinction that TiO_2 is not introduced during the process. The final product is identified as Bi_2WO_6. The 20-100 mg of the TB-x photocatalyst was then added to a 500 mL glass beaker containing 100 mL DI water and the HC filter. The suspension was ultrasonicated for 120 min, and the glass beaker was then placed in a convection oven operated at 85°C for 120 min to obtain the TB-x photocatalyst-loaded HC filter. Ultrasonication improved particle dispersion and promoted catalyst deposition within the porous HC channels, which enhanced contact between the catalyst and substrate. No binder was used to avoid pore blockage and active-site coverage. The coating stability was evaluated by repeated photocatalytic runs and post-reaction inspection, during which there was no apparent catalyst detachment or powder shedding.

2.3. Photocatalyst characterization

A suite of analytical techniques was employed to characterize the TB-x composites and reference materials (TiO_2 and Bi_2WO_6), probing their crystal structure, elemental composition, surface properties, morphologies, and optoelectronic properties. Fourier transform infrared spectroscopy (FTIR (Nicolet^{TM} iS50 FTIR spectrometer, Thermo Fisher Scientific, Waltham, Massachusetts, USA)) was utilized to identify the functional groups on the photocatalyst surfaces. The surface morphologies and the elemental distribution were analyzed using field emission scanning electron microscopy (SEM) fitted with an energy-dispersive X-ray spectroscopy (EDS) probe (Verios^{TM} 5 XHR, Thermo Fisher Scientific, Waltham, Massachusetts, USA). The high-resolution transmission electron microscope (HR-TEM) images were obtained using a JEM-2100F (JEOL Ltd., Tokyo, Japan). The surface properties (Brunauer-Emmett-Teller (BET) surface area and pore size distribution) of the tested photocatalysts were quantified using N_2 adsorption-desorption isotherms acquired at 77 K (3Flex, Micromeritics Instrument Corp., Norcross, Georgia, USA). The powder X-ray diffraction (PXRD) patterns (D8 ADVANCE, Bruker Corp., Billerica, Massachusetts, USA) were used to determine the crystal structures of the tested photocatalysts. The PXRD data were obtained in the 5-80° range using a scan speed and step size of 5° min^{-1} and 0.2°, respectively.

UV-Visible diffuse reflectance (UV-Vis-DRS) measurements performed over a range of 200-800 nm with Cary 5000 UV-Vis-near-infrared (NIR) spectrophotometer (Agilent Technologies, Inc., Santa Clara, California, USA) to characterize light absorption properties and photoluminescence (PL (FP-8200, Jasco International Co., Ltd., Tokyo, Japan)) spectroscopy were employed to determine the charge carrier recombination of the tested photocatalysts. X-ray photoelectron spectroscopy (XPS (K-alpha^{TM} system, Thermo Fisher

Scientific, Waltham, Massachusetts, USA)) was used to analyze the surface chemistry of the catalysts. The acquired XPS data were charge-corrected to 284.8 eV. An electrochemical workstation (VersaSTAT4, AMETEK Inc., Berwyn, Pennsylvania, USA) was employed to determine the transient photocurrent (PC) and electrochemical impedance spectra (EIS) of the tested photocatalysts. The electrochemical analysis was conducted in a three-electrode electrolytic cell with a quartz window. The working electrode consisted of TB-x coated fluorine-doped tin dioxide (FTO) conductive glass, the reference electrode was silver (Ag) / silver chloride (AgCl) (stored in 3.0 M KCl solution), and the counter electrode was a platinum (Pt) wire. The electrolyte was a 0.5 mol L^{-1} sodium sulfate (Na_2SO_4) solution. The external light source was a 10 W UV light-emitting diode (LED). The effective area of the working electrode was 2 cm × 2 cm area. The EIS was analyzed at an open circuit potential (1 V versus Ag/AgCl) with a frequency range of 0.01 Hz to 100 kHz. Likewise, the transient PC responses for photocatalysts were recorded at the potential of 1 V versus Ag/AgCl.

Electron paramagnetic resonance (EPR) spectrometry (EMXplus: Bruker Corp., Billerica, MA, USA) was used to evaluate the generated reactive oxygen species (ROS) (e.g., superoxide [$\cdot O_2^-$] and hydroxide [$\cdot$OH] radicals) during PCO using 5,5-dimethyl-1-pyrroline N-oxide (DMPO) as the spin-trapping agent. The adsorption and photocatalytic oxidation mechanisms of FA on the best-performing photocatalyst were investigated using *in-situ* DRIFTS (Nicolet^{TM} iS50, Thermo Scientific, USA) by tracking the evolution of surface UV light irradiation. This experimental sequence clarifies how the technique captures the dynamic transition from purely adsorbed intermediates to photoinduced reaction species and products.

2.4. Photocatalytic FA removal experiments

2.4.1. Setup and method

The experimental setup involved connecting the cord of the AP unit to a mobile power supply. A commercial FA sensor (TM-802, TENMARS Electronics Co., Ltd., Taipei, Taiwan (range: 0.01–5 ppm FA and 5–95 % RH and accuracy: ± 5 % of the reading (~ ± 0.03 ppm FA and ± 8% RH))) was placed near the AP unit for real-time monitoring of the varying FA concentration values within the chamber. The photocatalyst-loaded HC filter was installed in the AP unit. The chamber was flushed with air until the FA sensor registered at 0 ppm, after which a precise volume of DI H_2O and FA G-PS was introduced to maintain the selected RH levels inside the chamber. The photocatalytic oxidation of FA was conducted at room temperature (RT) and atmospheric pressure under UV irradiation (power = 0.98 W and λ_{max} = 371 nm). Subsequently, the FA removal performance of the best-performing TB-x photocatalyst was investigated as a function of various process variables such as m_{cat} (20-100 mg), AP flow rate (100-160 L min^{-1}), RH level (0-80%), FA concentration (1-5 ppm), O_2 content (0-21 vol.%), and reuse cycles.

The produced CO_2 concentration (for calculating the CO_2 yield (Y_{CO2})) was determined using a gas chromatograph (GC)-methanizer-flame ionization detector (FID) system (NexisTM GC-2030, Shimadzu Corp., Kyoto, Japan). The Y_{CO2} was quantified based on the CO_x signal in the chromatogram, as the photocatalytic FA oxidation experiments were conducted with an excess O_2 concentration (21 vol.%). The photocatalytic FA oxidation pathway was assessed using *in-situ* DRIFTS (Nicolet^{TM} iS50 FTIR spectrometer (Thermo Fisher Scientific, Waltham, Massachusetts, USA) equipped with a diffuse reflectance cell (Praying Mantis^{TM}, Harrick Scientific Products Inc., Pleasantville, New York, USA). For in-situ DRIFTS analysis, a higher FA concentration (100 ppm, G-WS in air or N_2 at 0% RH)

was employed to improve the detectability of adsorbed species and transient intermediates, which are often too weak to be resolved at trace-level concentrations. The photocatalyst (50 mg) was loaded into the cell and flushed with dry air at 100 mL min^{-1} for 60 min prior to measurement. Spectra were collected sequentially: (1) background spectrum of the flushed catalyst; (2) spectra under dark conditions after exposure to the FA stream (100 mL min^{-1}) to monitor adsorption; and (3) spectra under UV irradiation at fixed time intervals to track the evolution of surface intermediates and products. All spectras were acquired at room temperature using identical acquisition parameters, and dark/UV datasets were referenced to the same background to enable direct comparison. Although the surface coverage of intermediates at 100 ppm is expected to be higher than under lower, more realistic concentrations, the DRIFTS experiment was designed to identify the dominant surface reaction pathway rather than to replicate the exact surface conditions during actual photocatalytic operation. Therefore, the intermediate evolution observed at 100 ppm is used here for mechanistic assignment, while the practical photocatalytic performance was evaluated separately under lower formaldehyde concentrations in the air purifier (AP) chamber tests.

2.4.2. Data analysis

FA removal efficiency (X_{FA} (%)) was calculated using Eq. 1. The kinetic reaction rate (r (mmol h^{-1} g^{-1})) was calculated using Eq. 3. The Eqs. 4 and 5 were used to calculate the apparent quantum yield (AQY (%)) and mass-normalized apparent quantum yield (MAQY (molecules $photon^{-1}$ g^{-1})), respectively. The Eqs. 2, 6, and 7 were used to calculate the experimental decay constant (k_e), CADR (L min^{-1}), and specific CADR (SCADR, L min^{-1} g^{-1}), respectively. The Eq. 8 was utilized to calculate the Y_{CO2}. C_0 represents the initial FA

concentration. C_t denotes the FA concentration at a specific time point. k represents the decay constant (min^{-1}). k_e denotes the experimental decay constant obtained by the generalized reduce-gradient non-linear regression fitting using Eq. 2. V represents the volume of the chamber (24 L). $\Delta C/\Delta t$ represents the FA decay rate. R and T denote the universal gas constant and temperature, respectively. k_n indicates the natural decay rate constant. F is the photon flux per second on the HC filter. C_d indicates the CO_2 concentration at a specific time point. All experiments were conducted three times to ensure the reproducibility of the data. The error bars on the performance data indicate the standard deviation of triplicate runs.

$$X_{FA} = 100 * \frac{C_0 - C_t}{C_0} \quad \text{(Eq. 1)}$$

$$C_t = C_0 e^{-kt} \quad \text{(Eq. 2)}$$

$$r = 1000 * \frac{\Delta n}{m_{cat} * \Delta t} = 1000 * \frac{\Delta C * 10^{-6} * V}{m_{cat} * \Delta t * R * T} \quad \text{(Eq. 3)}$$

$$AQY = \frac{Decay\ rate}{Photon\ flux} \times 100 \quad \text{(Eq. 4)}$$

$$MAQY = \frac{AQY}{100 \times m_{cat}} \quad \text{(Eq. 5)}$$

$$CADR = V * (k_e - k_n) \quad \text{(Eq. 6)}$$

$$SCADR = \frac{CADR}{m_{cat}} \quad \text{(Eq. 7)}$$

$$Y_{CO_2} = 100 * \frac{C_d}{C_0 - C_t} \quad \text{(Eq. 8)}$$

2.5 DFT models and methods

All calculations were performed using density functional theory (DFT) as implemented in the Vienna Ab initio Simulation Package (VASP). The exchange-correlation functional was treated within the generalized gradient approximation using the Perdew-Burke-

Ernzerhof parameterization (GGA-PBE). Interactions between ion cores and valence electrons were described by the projector augmented wave (PAW) method. A plane-wave cutoff energy of 450 eV was applied throughout. The Brillouin zone was sampled using Monkhorst-Pack k-point meshes of 2 × 2 × 1 for structural relaxations and 2 × 2 × 1 for electronic property calculations (along the non-periodic direction). These choices ensure total-energy changes < 5 meV $atom^{-1}$ upon further k-point refinement. Structural relaxations were conducted until the Hellmann-Feynman forces converged to below 0.02 eV/Å and the total energy change fell below 10^{-5} eV per step, with an electronic (SCF) convergence threshold of 10^{-6} eV.

To construct the heterojunction, Bi_2WO_6 (131) and TiO_2 (101) slabs were brought into registry to maximize interfacial contact while minimizing lattice strain. The smaller in-plane cell was isotropically stretched to achieve a lattice mismatch of ≤ 3%. Each slab contained a thickness equivalent to two stoichiometric formula-unit stacking blocks and was separated by a 20 Å vacuum region to eliminate spurious interactions between periodic images. The bottom atomic layer of TiO_2 slab was fixed at bulk positions to mimic the support, while all other atoms in both slabs were fully relaxed. Because interfacial adhesion and adsorbate interactions involve dispersion forces. Grimme's DFT-D3 correction was applied to account for van der Waals interactions. GGA-PBE is known to underestimate band gaps. Therefore, single-point HSE06 hybrid-functional calculations were performed on the PBE-relaxed geometries to obtain more reliable band structures and projected densities of states (PDOS) for the analysis of optical/electronic properties. Band edges were referenced to vacuum using the planar-averaged electrostatic potential. From the optimized structures, we computed PDOS, work functions ($\Phi = V_{vac} - E_F$), and charge-density difference maps (CDD maps, $\Delta\rho = \rho(TiO_2\text{-}Bi_2WO_6) - \rho(Bi_2WO_6) - \rho(TiO_2)$. Electron localization functions (ELF)

and all isosurface visualizations were visualized with the VESTA package.

3. Results and discussion

3.1 Physicochemical characteristics

The successful formation of the TB-x composite (e.g., TB-5) was confirmed through structural and chemical analysis. HRTEM *(Fig. 1a-c)* revealed the coexistence of hexagonal TiO_2 and nanosheet-like Bi_2WO_6, with lattice fringes of 0.314 nm (Bi_2WO_6 (131)) and 0.351 nm (TiO_2 (101)) confirming intimate contact. SAED and SEM-EDS *(Fig. 1d, S1)* further verified the polycrystalline nature and uniform distribution of Bi_2WO_6 on the TiO_2 surface. BET analysis *(Fig. 2a-b, Table 1)* showed that pristine Bi_2WO_6 possessed the highest surface area (72.78 m^2/g), pore volume (0.17 cm^3/g), and pore size (5.22 nm) due to its layered structure. Composite formation reduced these textural parameters, likely due to pore blockage, with TB-10 retaining the highest porosity among the composites. The PXRD results for TB-x composite photocatalysts (e.g., TB-2, TB-5, TB-10) and their pristine counterparts (i.e., Bi_2WO_6 and TiO_2) are presented in *Fig. 2c*. The diffraction peaks of Bi_2WO_6 match well with its standard pattern (JCPDS 39-0256). In case of pristine Bi_2WO_6, the main peaks appear at 28.3°, 32.8°, 47.0°, 55.9°, 58.5°, 68.8°, 76.0° and 78.3° corresponding to the (131), (002), (202), (133), (262), (004), (391) and (204) crystal planes, respectively. These reflections are characteristic of orthorhombic Bi_2WO_6, confirming that the synthesized Bi_2WO_6 retains its well-defined orthorhombic crystal structure [30]. Likewise, the diffraction peaks of TiO_2 align with its standard patterns (JCPDS 21-1272 and JCPDS 21-1276), indicating the presence of TiO_2 in the anatase and rutile phases [12]. The preservation of such crystalline phases of both materials indicates high structural stability, which is essential for maintaining lattice integrity and facilitating efficient interfacial contact in the subsequent formation of the TB-x S-scheme heterojunction. In the case of TB-x

311 catalysts with higher Bi_2WO_6 content (i.e., TB-5 and TB-10), the characteristic Bi_2WO_6
312 diffraction peaks become more prominent in the XRD patterns *(Fig 2c)*.

313 Using the diffraction peak of TiO_2 (101) as reference, the crystallinity index (CI) of
314 pristine P25 was 99.4%. After heterojunction formation, the CI decreased to 98.5% for TB-
315 2, 98.0% for TB-5, and 97.7% for TB-10. CI value was calculated using the equation CI =
316 $(I_{max}-I_{back})/I_{max}*100$, where I_{max} is the highest intensity value of TiO_2 (101) and I_{back} is the
317 lowest intensity of PXRD pattern of catalyst. This gradual decline suggests that the
318 introduction of Bi_2WO_6 slightly disrupted the structural order of TiO_2, with the effect mainly
319 confined to the near-surface region. Notably, no obvious peak shift was observed in the
320 PXRD patterns (< 0.1°), indicating that the bulk crystal structure of TiO_2 remained
321 essentially unchanged, without significant lattice reconstruction or the formation of a new
322 crystalline phase. Therefore, the reduction in CI values is more reasonably attributed to local
323 interfacial disorder and microstrain generated during heterojunction formation, rather than
324 to a substantial change in lattice parameters. As the Bi_2WO_6 content increased, the interfacial
325 contact area between the two phases became larger, leading to the gradual accumulation of
326 surface stress in the TB-x samples. Such interfacial stress can reduce local crystallographic
327 order without causing a measurable peak shift. These results further suggest that the TB-x
328 samples are not simple physical mixtures but rather heterostructures with effective
329 interfacial coupling, and that the local lattice perturbation is mainly confined to the contact
330 region. This moderate interfacial disturbance is expected to favor interfacial charge
331 redistribution and internal electric field (IEF) formation, thereby facilitating charge transfer
332 across the heterojunction [12].

333 To elucidate the surface chemical state of the TB-5 heterojunction catalyst, X-ray

photoelectron spectroscopy (XPS) analysis was conducted with all binding energies (BE) calibrated against the C 1s reference at 284.80 eV. As presented in *Fig. 3a*, the Bi 4f XPS spectrum of Bi_2WO_6 exhibits two distinct peaks at 164.5 eV and 159.2 eV, corresponding to Bi $4f_{5/2}$ and Bi $4f_{7/2}$ states, respectively, while the TB-5 corresponding peaks shift to 164.3 and 159.0 eV [31]. This negative shift to lower binding energy indicates increased electron density around Bi species after heterojunction formation. In the case of pristine TiO_2, as illustrated in *Fig. 3b*, Ti 2p spectra display characteristic peaks at 464.2 eV and 458.5 eV for Ti $2p_{1/2}$ and Ti $2p_{3/2}$ transitions. In contrast, the Ti 2p spectra of TB-5 exhibit these peaks at 464.5 eV and 458.7 eV, manifesting a positive shift of 0.2 eV compared to pure TiO_2 [13]. This positive shift to higher binding energy indicates electron depletion around Ti sites. Taken together, the opposite shifts of Bi 4f and Ti 2p support interfacial electron transfer from TiO_2 to Bi_2WO_6 upon heterojunction formation. This charge redistribution establishes an IEF directed from TiO_2 toward Bi_2WO_6, driven by the equalization of Fermi levels across the interface [32]. The W 4f spectra of both Bi_2WO_6 and TB-5 presented in *Fig. 3c* show peaks at approximately 37.4 eV and 35.3 eV assigned to W $4f_{5/2}$ and W $4f_{7/2}$ states, with negligible shifts observed upon heterojunction formation, suggesting that the tungsten chemical state remains largely unchanged. Likewise, the O 1s spectra of pristine Bi_2WO_6 and TiO_2 materials (*Fig. 3d)* display a prominent peak at 531.8 eV corresponding to surface-adsorbed oxygen (O_{ads}) species without detectable shifts following composite formation (i.e., TB-5). The lattice oxygen (O_{latt}) peaks of Bi_2WO_6, TiO_2, and TB-5 appeared at 530.1, 529.9, and 530.0 eV, respectively [33]. The absence of an obvious shift in the O_{ads} peak does not contradict the interfacial charge redistribution observed from Bi 4f and Ti 2p. This is because the broad components (including surface hydroxyls, adsorbed water, and weakly bound oxygen species) have average binding energy that is less sensitive to localized

interfacial electron transfer than the metal core levels. In comparison, the slight shift in lattice oxygen suggests that the oxygen environment is affected to a limited extent, while the dominant charge redistribution occurs mainly around the interfacial Bi and Ti sites. The survey spectra presented in *Fig. 3e* demonstrate that TB-5 contains the constituent elements Bi, W, Ti, and O, confirming successful integration of the Bi_2WO_6 and TiO_2.

The UV-Vis DRS spectrum *(Fig. 4a)* shows that TiO_2 exhibits strong absorption in the ultraviolet range (≈ 200 – 363 nm) with a light absorption edge at ~310 nm. In contrast, Bi_2WO_6 absorbs strongly from ≈ 200 – 388 nm with a light absorption edge near ~ 330 nm, and its intensity extends further into the visible region. The electronic structures of the two materials differ significantly. TiO_2 possesses a large band gap, confining its light absorption to the ultraviolet spectrum [34]. In contrast, the VB of Bi_2WO_6, formed by O 2p orbitals from the $[BiO]^+$ layers, lies at a higher energy, resulting in a narrower bandgap and a visible-light-responsive absorption edge [35]. Upon TB-x (x = 2, 5, and 10) heterojunction materials, the light absorption edges shift to longer wavelengths. Specifically, compared to pure TiO_2, the light absorption edges for TB-2, TB-5, and TB-10 are red-shifted to approximately 315, 317, and 319 nm, respectively. This phenomenon is consistent with the alignment of Fermi-levels at the contact interface, which generates an IEF. The IEF creates band bending and interfacial charge-transfer states [36]. These factors collectively extend the spectral response and could increase the generation rate of electron-hole pairs. Correspondingly, the Tauc plots *(Fig. 4b)* indicate that the optical band gaps of TB-2, TB-5, and TB-10 are smaller than that of TiO_2, reaching around 3.04, 3.06, and 3.08 eV, respectively.

Both Bi_2WO_6 and TiO_2 are confirmed as n-type semiconductors through the Mott-

Schottky (M-S) curve analysis (Eq. 10, *Fig 4c)*, evidenced by the positive slopes of their respective $1/C^2$ versus potential plots [37]. This electronic structure characterization reveals a key distinction: TiO_2's large bandgap confines its absorption to the ultraviolet spectrum, whereas the VB maximum in Bi_2WO_6 lies at a higher energy owing to O 2p orbitals. This results in a narrower bandgap and subsequent visible-light photoabsorption.

$$\frac{1}{C^2} = \frac{2}{\varepsilon \times \varepsilon_0 \times e \times N_d} \times \left(E - E_{FB} - \frac{KT}{e}\right) \quad \text{(Eq. 10)}$$

Where C, ε, ε_0, e, N_d, E, E_{FB}, K, and T represent the space charge capacitance ($cm^4\ F^{-2}$), dielectric constant, vacuum dielectric constant (8.86×10^{-14} F/cm), donor density (cm^{-3}), applied potential (V Ag/AgCl), flat band potential (V Ag/AgCl), Boltzmann constant (1.38×10^{-23} J K^{-1}), and temperature (K) of n-type semiconductor, respectively [38]. The E_{FB} values of Bi_2WO_6 and TiO_2 were determined from M-S analysis of EIS measurements to be -0.21 and -0.64 V vs. Ag/AgCl, respectively. Subsequently, the Nernst equation was used to convert these E_{FB} values into the normal hydrogen electrode (NHE) scale (Eq. 11).

$$E_{FB}(NHE) = E^{\theta}\left(\frac{Ag}{AgCl}\right) + E_{FB}\left(\frac{Ag}{AgCl}\right) + 0.059 \times pH \quad \text{(Eq. 11)}$$

E^{θ} (Ag/AgCl) is 0.197 V. For n-type semiconductors, the E_{FB} is generally located at a potential ~0.2 eV more positive than the conduction band minimum (E_{CB}). Therefore, E_{CB} positions of both Bi_2WO_6 and TiO_2 were calculated using the equation $E_{CB} = E_{FB}(NHE) - 0.2$, which are determined to be -0.213 and -0.643 eV (vs. NHE), respectively. Finally, the valence band maximum (E_{VB}) positions were computed from the optical band gaps (E_g) and the calculated E_{CB} values via the relation $E_{VB} = E_g + E_{CB}$. Thus, the CB and VB positions of Bi_2WO_6 and TiO_2 are established as -0.213/2.767 V vs NHE and -0.643/2.537 V vs NHE, respectively *(Fig. 5a)*.

403 The formation of ROS, particularly hydroxyl radicals (·OH) and superoxide radicals
404 ($\cdot O_2^-$), is critical, as these species are the primary oxidative agents responsible for the
405 breakdown and ultimate mineralization of FA into CO_2 and H_2O. The ·OH radical is known
406 as one of the most powerful oxidizing agents in aqueous and surface chemistry. It attacks
407 non-selectively, cleaving the C-H bonds of adsorbed FA and its intermediate species (e.g.,
408 dioxymethylene (DOM) and formate). Concurrently, the $\cdot O_2^-$ radicals contribute to the
409 oxidative degradation chain and help suppress the recombination of photogenerated
410 electron-hole pairs.

411 The potential for generating these ROS is directly governed by the semiconductor's band
412 structure *(Fig. 5)*. For the efficient production of surface-bound ·OH radicals, which is
413 crucial for gas-phase photocatalysis, the VB potential must be sufficiently positive to oxidize
414 surface hydroxyl groups (-OH) or adsorbed water (H_2O). This is quantified by the
415 thermodynamic requirement that the VB potential must be more positive than the standard
416 oxidation potential of $H_2O/\cdot OH$ (+2.72 to 2.99 eV vs. NHE) or, more practically for surface-
417 adsorbed species, $OH^-/\cdot OH$ (+1.99 eV vs. NHE). Therefore, a key material property for
418 efficient gas-phase ·OH radical generation is VB potential significantly more positive than
419 +2.0 eV vs. NHE. This energetic configuration enables the photogenerated holes (h^+) to
420 oxidize ubiquitous surface-adsorbed hydroxyl ions (OH^-) into gaseous ·OH radicals. These
421 radicals then diffuse from the catalyst surface to initiate the oxidative degradation of FA
422 molecules in the adjacent gas phase, making this interfacial ·OH shuttle a critical step for
423 the PCO of air pollutants.

424 The work function difference ($\Delta\Phi$) is a critical parameter for offering valuable insights
425 into the interfacial charge transfer mechanism in heterojunction catalysts. The $\Delta\Phi$ values of

Bi_2WO_6 and TiO_2 were determined experimentally using UPS.

$$\Delta\Phi = hv - (E_{cutoff} - E_{edge}) \quad \text{(Eq. 12)}$$

where *hv* represents the incident photon energy (21.22 eV). The secondary electron cutoff energy (E_{cutoff}) and the Fermi edge (E_{edge}) of Bi_2WO_6 (18.39/2.66 eV) and TiO_2 (16.96/0.88 eV) were determined from the UPS spectra *(Fig. 4d-e)*, therefore the ΔΦ values of Bi_2WO_6 and TiO_2 can be determined as 5.48 and 5.13 eV based on Eq. 12, respectively. Furthermore, the Fermi levels (E_f) relative to the NHE of Bi_2WO_6 and TiO_2 were computed as 1.04 and 0.69 eV, respectively according to the equation, NHE = ΔΦ - 4.44. Before two types of semiconductors contact, the Fermi level of each semiconductor remains independent and the band positions are determined solely by their intrinsic electronic structures *(Fig. 5a)*. After contact under equilibrium conditions, this energy alignment drives electron transfer at the interface, inducing upward band bending (electron depletion) in TiO_2 and downward band bending (electron accumulation) in Bi_2WO_6. Consequently, an IEF directed from TiO_2 to Bi_2WO_6 is established across the TB-5 heterojunction catalysts *(Fig. 5b)* [39]. The charge transfer pathway in the TB-5 heterojunction is conclusively determined by its electronic structure, so that the staggered band alignment of TB-5 could theoretically support a type II or an S-scheme heterojunction [40,41]. However, the key distinction lies in the fate of the photogenerated charge carriers. In a type-II heterojunction, e^- in the CB of Bi_2WO_6 transfer to the CB of TiO_2, while h^+ in the VB of TiO_2 migrate to the VB of Bi_2WO_6. This pathway promotes spatial charge separation but weakens the overall redox ability. By contrast, in the S-scheme pathway, the IEF and Coulombic attraction drive the recombination of low-energy e^- in the CB of Bi_2WO_6 with low-energy h^+ in the VB of TiO_2. As a result, high-energy e^- and h^+ remain in the CB of TiO_2 and in the VB of Bi_2WO_6, respectively. This charge-transfer

route preserves the strong reduction and oxidation capacities required for ROS generation and FA mineralization. Thus, despite the staggered band alignment, TB-5 retains an S-scheme mechanism (rather than forming a type-II heterojunction), as evidenced by the work function difference, interfacial band bending, and retention of strong redox potentials [13] *(Fig. 5c)*.

In addition, the generation of ROS species from TB-5 under UV on/off conditions were evaluated using EPR spectroscopy (*Fig. 6a*). The absence of signals corresponding to $\cdot O_2^-$ and ·OH under dark conditions indicates that no ROS were generated during the adsorption process. In contrast, after 5 minutes of UV irradiation, the EPR spectra of TB-5 exhibited 6 characteristic peaks of $\cdot O_2^-$ at 3476.2, 3484.2, 3489.5, 3498.0, 3503.7, and 3511.7 G and four characteristic peaks of ·OH at 3474.0, 3488.1, 3503.2, and 3518.1 G. These results demonstrate that $\cdot O_2^-$ and ·OH are generated by TB-5 under UV light, which can effectively promote the degradation of FA [42].

Electrochemical analysis, such as EIS and PC, effectively evaluates conductivity and charge transfer [43]. As shown in *Fig. 6b*, TB-5 has the lowest charge transfer resistance (3.35 Ω), which is 1.97 to 0.31 times lower than the other ones. Consistently, the PC of TB-5 is the highest (86 μA cm^{-2}), which is 4.30 to 1.15 times higher than Bi_2WO_6, TiO_2, TB-2, and TB-10, respectively (*Fig. 6c)*. This demonstrates that TB-5 has superior charge separation and light responsiveness, resulting in excellent photocatalytic performance [44]. The charge separation efficiency was further confirmed by PL spectroscopy *(Fig. 6d)*. A lower PL intensity signifies suppressed electron-hole recombination, as the emission stems from charge carrier recombination. [45]. In contrast, the reduced PL intensity of TB-x compared with pure TiO_2 reflects carrier-recombination processes modulated by the

heterojunction interface [46]. Among the heterojunction catalysts, TB-5 exhibited the PL intensity, aligning with the EIS and PC results and affirming its excellent charge separation capability.

3.2 FA removal performance of TB-x photocatalysts and parameter-dependent behavior of TB-5

The photocatalytic performance evaluation results demonstrate that TB-x composite photocatalysts exhibit significantly superior FA degradation efficiency compared to TiO_2. *Fig. 7a* illustrates the temporal relationship between the X_{FA} and the tested photocatalysts' performance. Under 360 s of illumination, the X_{FA} of TB-x photocatalysts displayed the order of: TB-5 (93.6%) > TB-10 (92.0%) > TB-2 (82.2%) > TiO_2 (76.9%) > Bi_2WO_6 (56.6%) (*Fig. 7a*). This contrasts greatly with UV off condition in which Bi_2WO_6 shows the maximum X_{FA} (39.5%). When the reaction time is extended to 780 s, the TB-x composite photocatalysts achieved complete mineralization of FA (X_{FA} = 100%), while TiO_2 and Bi_2WO_6 only reached 98.7 and 56.6%, respectively. Among them, TB-5 demonstrated the best FA removal performance, with a SCADR of 123.80 L min^{-1} g^{-1}, which is 1.9 times better than TiO_2 (59.51 L min^{-1} g^{-1}) and 3.5 times better than Bi_2WO_6 (32.25 L min^{-1} g^{-1}) (*Table 2*). Furthermore, TB-5 also showed the highest r_{10}, r_{max}, AQY, and MAQY value of 1.72 mmol g^{-1} h^{-1}, 0.35 mmol g^{-1} h^{-1}, 2.68E-01% and 3.20E-02 molecules $photon^{-1}$ g^{-1}, which is 1.5, 1.6, 1.3, and 1.6 times better than TiO_2 and 2.3, 2.7, 2.3, 2.6 times better than Bi_2WO_6. Overall, all performance indicators confirmed that TB-5 is the most effective catalyst for FA degradation. Therefore, our study selects TB-5 as the optimal photocatalyst for a subsequent systematic investigation of the influence of various process parameters on FA degradation. It should be noted that the higher AQY and reaction rates observed at 5 ppm reflect a higher instantaneous utilization of active sites and photogenerated charge carriers under emission-

level conditions, rather than a loss of practical applicability at lower concentrations. At lower FA levels, the absolute reaction rate and photon utilization decrease because fewer FA molecules are available to occupy surface active sites. Nonetheless, the catalyst can still achieve rapid purification owing to the lower pollutant burden, as reflected by the higher CADR/SCADR values obtained at 1 ppm. In this sense, the concentration dependence indicates a shift in the dominant performance metric: rate-based and quantum-yield descriptors are maximized at higher FA concentrations, whereas air-cleaning efficiency is enhanced more favorably at lower concentrations.

The presence of relative humidity (RH) significantly influences the photocatalytic performance of catalysts, while its catalytic oxidation mechanism for VOCs is relatively complex [47]. As shown in *Fig. 7b*, increasing environmental RH levels significantly reduced the X_{FA} of TB-5. At 600 s, X_{FA} showed a decreasing trend of: 0% RH (100%) > 20% RH (98.63%) > 50% RH (83.67%) > 80% RH (74.80%). Specifically, the CADR/SCADR also exhibited a clearly decreasing trend with increasing RH: 0% RH (10.37 L min^{-1}/123.80 L min^{-1} g^{-1}) > 20% RH (6.15 L min^{-1}/73.35 L min^{-1} g^{-1}) > 50% RH (3.38 L min^{-1}/40.36 L min^{-1} g^{-1}) > 80% RH (2.33 L min^{-1}/27.76 L min^{-1} g^{-1}) (*Table 2*). Similarly, r_{10}, r_{max}, AQY, and MAQY values showed the same trend with X_{FA}. Specifically, the r_{10}/MAQY values (1.77 mmol g^{-1} h^{-1}/3.20E-02 molecule $photon^{-1}$ g^{-1}) of TB-5 at 0% RH were approximately 0.7/0.2, 1.8/0.4, and 2.3/0.7 times higher than those of the 20, 50, and 80% RH, respectively. This phenomenon can be explained by the competitive relationship between FA molecules and H_2O on the surface of TB-5 [48]. In a humid environment, H_2O molecules may form a thin water film on the surface of TB-5, blocking active sites and inhibiting FA mineralization [49].

519 Furthermore, this study systematically investigated the effects of catalyst mass (20-100
520 mg) and initial FA concentration (1-5 ppm) on the FA removal performance of TB-5. As
521 shown in *Fig. 7c*, the X_{FA} of TB-5 significantly improved with an increasing catalyst mass.
522 At 600 s, XFA of TB-5 with different mass shows a trend of: 100 mg (100%) > 50 mg
523 (98.1%) > 20 mg (31.41%). TB-5 exhibited the best performance under 100 mg mass
524 loading, with a CADR value, SCADR value, and AQY value reaching 10.37 L min^{-1}, 123.80
525 L min^{-1} g^{-1}, and 2.68E-01 %, respectively. Additionally, the MAQY value (i.e., 4.85E-02
526 molecule $photon^{-1}$ g^{-1}) of TB-5 with 50 mg was 1.4 times that of 20 mg and 1.5 times that of
527 100 mg, respectively *(Table 2)*. This can be attributed to the higher catalyst mass providing
528 more active sites, thereby promoting FA removal (Hua et al., 2024).

529 The effect of initial FA concentration on the performance of TB-5 is also plotted in *Fig.*
530 *7d*. Within 600 s, TB-5 could achieve complete degradation of FA (X_{FA}=100%) across
531 various initial FA concentrations (1-5 ppm). This study found that the CADR and SCADR
532 values decreased with increasing FA concentration, showing the following trend: 1 ppm
533 (21.09 L min^{-1}/251.65 L min^{-1} g^{-1}) > 3 ppm (11.94 L min^{-1}/142.51 L min^{-1} g^{-1}) > 5 ppm (10.37
534 L min^{-1}/123.80 L min^{-1} g^{-1}). However, the r_{10}, AQY, and MAQY values exhibited an opposite
535 trend: 1 ppm (0.41 mmol g^{-1} h^{-1}/1.79E-01%/2.13E-02 molecule $photon^{-1}$ g^{-1}) < 3 ppm (1.12
536 mmol g^{-1} h^{-1}/2.68E-01 %/3.20E-02 molecule $photon^{-1}$ g^{-1}) < 5 ppm (1.77 mmol g^{-1} h^{-1}/2.68E-
537 01 %/3.20E-02 molecule $photon^{-1}$ g^{-1}). The observed trends occur because CADR/SCADR
538 and r_{10}/AQY/MAQY measure different aspects of performance. The system is most efficient
539 at cleaning air (high CADR) at low concentrations because the fixed number of active sites
540 on the catalyst can rapidly reduce a dilute pollutant level to zero. Conversely, it is most active
541 and utilizes light best (high r_{10}, AQY, MAQY) at high concentrations because the abundant
542 FA molecules ensure the catalyst's active sites are constantly occupied and working at their

maximum capacity. This higher reactant concentration drives a greater absolute number of degradation events per unit time and improves the quantum yield by outcompeting inherent electron-hole recombination [9].

The influence of key operational parameters on the photocatalytic performance of the optimal TB-5 catalyst was also investigated in terms of flow rate, O_2 levels, and synthesis conditions. As illustrated in *Fig. 7e* and summarized in *Table 2*, an increase in the air purification flow rate from 100 to 160 L min^{-1} led to a consistent enhancement in all performance metrics, including X_{FA}, SCADR, and r_{10}/r_{max}. This uniform improvement is attributed to enhanced mass transfer in the AP system with continuous recirculation of feed gas, which facilitates faster contact between FA molecules and the catalyst's active sites [50]. Similarly, the concentration of O_2 was found to be critically important, as demonstrated in *Fig. 7f* and *Table 2*. All evaluated metrics, X_{FA}, SCADR, r_{10}, r_{max}, and MAQY, exhibited a strong, positive correlation with increasing O_2 concentration. This clear trend underscores the essential role of molecular oxygen as a primary electron scavenger for the generation of ROS, such as $\cdot O_2^-$, which are vital for the oxidative degradation of FA [51]. In contrast to the uniform trends observed for flow rate and O_2, the effect of hydrothermal synthesis duration (6, 15, and 48 h) on the TB-5 series revealed a more complex relationship, as shown in *Fig. 7g* and *Table 2*. The X_{FA} and specific activity metrics (SCADR and AQY) were maximized for the material prepared with an intermediate duration, TB-5 , indicating that this condition achieves an optimal balance between the crystallinity of Bi_2WO_6 and the phase composition of TiO_2 for effective S-scheme charge transfer [52,53]. Interestingly, the CADR results followed a different trend as TB-5 prepared over 6 hours (i.e., the shortest synthesis duration) exhibited the highest value (*Table 2*). This divergence highlights a nuanced trade-off, where insufficient crystallization time may yield a high initial surface

area but compromises the electronic interaction crucial for long-term heterojunction stability and quantum efficiency.

3.3 Reusability of photocatalyst and FA mineralization

To evaluate the stability of TB-5, FA PCO experiments were repeated five times using 5 ppm FA. After 5 cycles (each cycle over 13 minutes), TB-5 was still able to achieve 100% of X_{FA}. Moreover, no significant decline in the values of CADR, SCADR, r_{10}, r_{max}, AQY, and MAQY *(Table 2)* indicates that TB-5 possesses excellent stability and potential for practical applications. The photocatalytic mineralization performance of TB-5 toward FA vapor was also assessed by monitoring CO_2 evolution *(Fig. S2)*. Under UV irradiation at 0% RH, in a single run with an initial FA concentration of 100 ppm for 120 min, X_{FA} of TB-5 could reach 96.6% while Y_{CO2} attained 81.6%. These results demonstrate that TB-5 exhibits high degradation activity and mineralization capability toward FA.

3.4 Photocatalytic FA oxidation pathway and mechanism

3.4.1 *In-situ* DRIFTS

To reveal the specific reaction pathway of FA degradation by TB-5, we performed the *in-situ* DRIFTS analysis (*Fig. 8*). The spectral evolution under different conditions provides critical kinetic insights into the surface reaction mechanism. Initial adsorption under dry and dark conditions is shown in *Fig.8a*. The interaction of FA molecules with the TB-5 surface facilitated the formation of DOM, as confirmed by a peak at 1114 and 1268 cm^{-1}. Peaks at 1721 cm^{-1} (C=O stretching vibration of FA) was also observed [54]. The rapid formation of DOM in the dark indicates strong chemisorption even without photo-activation. Moreover, the negative band near 3570 cm^{-1} indicates the loss of pre-existing surface-bridging hydroxyl groups (-OH) relative to the hydrated background spectrum. During the subsequent dry purge, these -OH species are consumed, leading to a decrease in their absorbance. The

spectral changes confirm that the highly reactive TB-5 surface drives the transformation of DOM into $HCOO^-$ species.

The spectral evolution provides critical kinetic insights into the surface reaction. The initial rapid formation of DOM in the dark *(Fig. 8a)* suggests strong chemisorption and interaction of FA with the catalyst surface, even without photo-activation. Upon UV irradiation *(Fig. 8b)*, the marked increase in $HCOO^-$ bands (1558 and 1350 cm^{-1}) concurrent with the stabilization of DOM peaks indicates that the conversion of adsorbed DOM to $HCOO^-$ is a key photo-driven step. The introduction of humidity *(Fig. 8c)* significantly accelerates the depletion of DOM signals while further decreasing $HCOO^-$ peaks. It thus suggests that water plays a dual role: it not only generates a higher flux of ·OH radicals that attack DOM but may also facilitate the hydrolysis of this intermediate. The accumulation of $HCOO^-$ species under all conditions implies that its subsequent oxidation to CO_2 and H_2O is likely the rate-limiting step in the overall mineralization pathway. This detailed mechanistic understanding, moving from initial adsorption to the final kinetic bottleneck, is crucial for future strategies aimed at optimizing catalyst surface chemistry to enhance $HCOO^-$ decomposition.

Under UV irradiation at 0% RH level, the marked increase in formate bands at 1558 cm^{-1} and 1350 cm^{-1} concurrent with the stabilization of DOM peaks indicates that the photo-driven conversion of DOM to $HCOO^-$ is a key step (*Fig. 8b*). The introduction of 20% RH *(Fig. 8c*) significantly changed the evolution of surface intermediates. Both the DOM and $HCOO^-$ bands decreased in intensity, while the -OH band near 3570 cm^{-1} increased progressively. This result indicates that water participates in the surface reaction process and modifies the surface coverage of FA-derived species. However, in line with the chamber-

scale results, humidity did not improve the overall FA removal performance, indicating that any local participation of water in surface reactions is outweighed by its inhibitory effect on photocatalytic oxidation.

3.4.2 DFT simulation

To elucidate the electron-transfer mechanism in TB-5, density-functional calculations were performed to analyze the band structures, densities of states, work functions, electron-localization function (ELF)and charge-density difference of Bi_2WO_6, TiO_2, and the TB-5 heterostructure. The calculated band gaps of Bi_2WO_6, TiO_2, and the TB-5 heterojunction are 1.51, 2.54 and 1.61 eV, respectively *(Fig. 9a–c)*. The intermediate value observed for TB-5 reflects the combined electronic character of its constituents. As expected for GGA calculations, all values are slightly lower than the experimental data, owing to the known tendency of this approximation to underestimate semiconductor band gaps [55]. The projected DOS of TB-5 *(Fig. 9d–f)* suggests that its CBM and VBM are dominated by the Ti 3d states of TiO_2 and the O 2p states of Bi_2WO_6, respectively. Crucially, the DFT-calculated $\Delta\Phi$ values are 8.619 eV for Bi_2WO_6 and 7.258 eV for TiO_2. The discrepancy in $\Delta\Phi$ values arises primarily from the surface-sensitive nature, which depends strongly on slab thickness, vacuum spacing, surface termination, relaxation, and the presence of defects or adsorbates. The $\Delta\Phi$ values derived from UPS are often lower than the DFT-calculated because the catalyst surface is readily affected by contamination under experimental conditions. Therefore, while the absolute values differ, the relative trend remains physically meaningful and can still be used to identify the direction of interfacial charge transfer [56].

This significant difference in $\Delta\Phi$ values between the two components of heterojunction ($\Phi(Bi_2WO_6) > \Phi(TiO_2)$, *Fig 10a-b*) predicts that upon contact, electrons will flow from TiO_2 to Bi_2WO_6 until their Fermi levels equilibrate [57]. This process generates an IEF directed

from TiO_2 to Bi_2WO_6, which is the fundamental driving force for the S-scheme mechanism as discussed above in detail. While the absolute DFT values may deviate from experiment due to the use of idealized models and semilocal functionals, the relative trend is physically meaningful and aligns with our UPS results *(Fig. 4d-e)*. This theoretical framework is powerfully corroborated by experimental evidence. The predicted electron transfer is directly observed in the XPS spectra *(Fig. 3a-b)*, which shows a 0.2 eV blue shift for Ti 2p peaks (electron depletion) and a 0.2 eV red shift for Bi 4f peaks (electron accumulation). Furthermore, the charge-density-difference map calculated via DFT (*Fig. 10d*) visually confirms this spatial charge redistribution with electron accumulation on Bi_2WO_6 (yellow) and depletion on the TiO_2 side (cyan). In summary, the seamless alignment between DFT predictions and multiple experimental (e.g., XPS and UPS) methods provides a multi-faceted and unequivocal validation of an S-scheme charge transfer pathway in the TB-5 heterojunction.

3.4.3 Photocatalytic mechanism of FA

Based on the *in-situ* DRIFTS results and photoelectrochemical analysis, the oxidation pathway of FA at the surface of TB-5 S-scheme heterojunction can be explained via the following sequence of reactions [58,46]. The initial step involves the adsorption and surface reaction of FA, where *in-situ* DRIFTS confirmed the formation of a dioxymethylene (DOM, $[H_2CO_2]_{ads}$) intermediate. The subsequent steps are driven by the efficient charge separation of the S-scheme heterojunction, which provides a high flux of holes (h^+) for ·OH radical production and electrons (e^-) for $\cdot O_2^-$ generation, as evidenced by the strong photocurrent response and EIS data.

$$HCHO + O_{ads} \rightarrow [H_2CO_2]_{ads} \quad \text{(Eq. 13)}$$

$$TB-5+hv \rightarrow TB-5\,(e^- + h^+) \quad \text{(Eq. 14)}$$

$$OH^- + TB-5\,(h^+) \rightarrow \cdot OH \quad \text{(Eq. 15)}$$

$$O_2 + TB-5(e^-) \rightarrow \cdot O_2^- \quad \text{(Eq. 16)}$$

$$[H_2CO_2]_{ads} + \cdot O_2^- \rightarrow HCOO^- + OH^- \quad \text{(Eq. 17)}$$

$$[H_2CO_2]_{ads} + \cdot OH \rightarrow HCOO^- + H_2O \quad \text{(Eq. 18)}$$

$$HCOO^- + \cdot O_2^- + 2h^+ \rightarrow H_2O + CO_2 \quad \text{(Eq. 19)}$$

$$HCOO^- + \cdot OH + h^+ \rightarrow H_2O + CO_2 \quad \text{(Eq. 20)}$$

3.5 Performance comparison between different catalysts

To contextualize the performance of the TB-5 S-scheme heterojunction, its photocatalytic activity was benchmarked against other representative photocatalysts reported for gas-phase formaldehyde oxidation. The comparison, detailed numerically in *Table 3*, evaluates key performance indicators, including r_{max}, AQY, MAQY, and CADR under comparable conditions. An analysis of the intrinsic and practical kinetic descriptors reveals its superior performance.

The intrinsic kinetic capability of each catalyst was evaluated using the mass-normalized rate, r_{max} (mmol mg^{-1} h^{-1}). The top five materials of r_{max} rank as follows: N-TiO_2 (0.65) > TB-5 (0.31) > TiO_2-SiC (0.21) > NiO–TiO_2 (0.183) > Cu–TiO_2 (0.07) (*Table 3*). In terms of r_{max}, which reflects the intrinsic activity per mass of catalyst, TB-5 is a top-tier material, outperforming only by N-TiO_2.

The CADR (L min^{-1}) represents a standardized, device-level parameter that characterizes the practical throughput of an air purifier system, making it a crucial metric for

benchmarking real-world applicability. Comparison of CADR demonstrates TB-5's practical superiority. TB-5 achieves a CADR of 21.09 L min^{-1} at 1 ppm and 10.37 L min^{-1} at 5 ppm, the highest value among the catalysts evaluated. This performance significantly surpasses that of all other catalysts under low-concentration conditions. This establishes that while TB-5 has exceptional intrinsic kinetics, its practical cleaning efficiency is unmatched. Furthermore, the data highlights a key limitation of CADR: it exhibits a strong inverse relationship with initial FA concentration, as seen with TB-5, TiO_2-SiC, and NiO-TiO_2, whose CADR values drop substantially when concentration increases from 1 to 5 ppm.

Finally, the trend in kinetic superiority is corroborated by the AQY. AQY represents a practical tool for gauging photocatalyst effectiveness while providing essential metrics for cross-comparison among experiments conducted under various conditions [59]. Here, TB-5 developed in this work is found as the top-performing performer for AQY (%), while a similar relative trend is observed: N-TiO_2 (3.54×10^{-1}) > TB-5 (2.68×10^{-1}) > TiO_2-SiC (1.90×10^{-1}) > NiO–TiO_2 (1.36×10^{-1}) > $BiVO_4$ OVs–MIL-88A(Fe) (1.47×10^{-3}). To address the limitation that AQY omits catalyst mass considerations, MAQY (molecules $photon^{-1}$ g^{-1}) is presented alongside, offering a mass-weighted photonic efficiency parameter. The MAQY ranking follows the same order: N-TiO_2 (5.90×10^{-2}) > TB-5 (3.20×10^{-2}) > TiO_2-SiC (1.90×10^{-2}) > NiO–TiO_2 (1.62×10^{-2}) > Cu–TiO_2 (9.70×10^{-3}). Here, TB-5 (3.20×10^{-2}) at 5 ppm again ranks second only to N-TiO_2, confirming its high efficiency in converting light into chemical activity.

Collectively, the performance evaluation based on these key metrics demonstrates that TB-5 generally achieves outstanding FA removal across the full spectrum of evaluation criteria. The leading CADR value translates this material-level excellence into a practical,

device-level performance advantage. Further, high r_{max} also supports its intrinsic kinetic superiority at the material level. In addition, the outstanding AQY demonstrates its exceptional efficiency in converting photons into chemical reactions. In summary, TB-5 consistently ranks as one of the most kinetically capable and efficient photocatalysts, with its standout advantage being the highest practical CADR at low, realistic pollutant levels. This comprehensive outperformance indicates that TB-5 effectively integrates rapid surface kinetics with efficient photon-to-molecule conversion and high device-level throughput, establishing it as a truly promising catalyst for real-world applications.

4. Conclusions

In this study, a well-defined TiO_2-Bi_2WO_6 S-scheme heterojunction (TB-5) was successfully engineered and demonstrated outstanding capability for gaseous formaldehyde (FA) abatement. Photoelectrochemical measurements revealed that TB-5 exhibited higher photocurrent density (86 μA cm^{-2}) and lower charge-transfer resistance (3.35 Ω) than TiO_2 (24 μA cm^{-2}, 5.60 Ω) or Bi_2WO_6 (20 μA cm^{-2}, 6.60 Ω Under 0.98 W UV irradiation in a portable air-purification reactor, TB-5 could achieve 100% X_{FA} within 600 s, with a CADR value of 10.37 L min^{-1} and a SCADR value of 123.80 L min^{-1} g^{-1}, respectively. The AQY/MAQY also showed the highest value of 2.68E-01% and 3.20E-02 molecules $photon^{-1}$ g^{-1}, which is 2.3/2.6 times and 1.3/1.6 times better than its pristine components of Bi_2WO_6 and TiO_2, respectively. This enhanced performance is attributed to the formation of a highly efficient S-scheme heterojunction at the TB-5 interface, which preserves strongly oxidative holes in the Bi_2WO_6 VB and highly reductive electrons in the TiO_2 CB, thereby maximizing ROS ($\cdot O_2^-$/$\cdot$OH) generation and utilization. This unique charge transfer pathway not only accelerates FA oxidation kinetics but also ensures the retention of strong redox capability

essential for complete mineralization. This catalyst exhibited sustained activity over 5 cycles and maintained optimal performance at moderate hydrothermal synthesis durations (15 hours), confirming both structural and electronic robustness. *In-situ* DRIFTS analysis elucidated the photocatalytic oxidation for TB-5 via a clear stepwise pathway, which proceeds through three sequential steps: (i) FA adsorption on the surface ·OH of TB-5, (ii) adsorbed FA converts to DOM, followed by reaction with ROS to yield formate intermediates ($HCOO^-$), and (iii) complete mineralization to CO_2 and H_2O. Through the integration of experimental characterization and DFT modeling, we have validated the heterostructure design and elucidated the underlying charge transfer mechanism governing the enhanced photocatalytic activity of TB-5. Although this study is still limited by its evaluation under controlled laboratory conditions with single-component FA and UV-driven operation, these findings are inspired to establish formidable future optimization strategies for the efficient abatement of indoor VOCs.

Funding

This work was supported by a grant from the National Research Foundation of Korea (NRF) funded by the Ministry of Science and ICT (MSIT) of the Korean government (Grant No: 2021R1A3B1068304).

Reference

1. Bourguignon M, Grignard B, Detrembleur C (2021) Introducing Polyhydroxyurethane Hydrogels and Coatings for Formaldehyde Capture. ACS Applied Materials & Interfaces 13:54396-54408.
2. Wang T, Wang H, Xia P, Xue S, Yang G, Li H, Li Z, Jiang X, Xing X (2021) PVA-SM microstructure enhanced ratiometric fluorescence probe for formaldehyde detection in solution and gas. Opt. Lett. 46:5759-5762.
3. Hu D, Tobon Y, Agostini A, Grosselin B, Chen Y, Robin C, Yahyaoui A, Colin P, Mellouki A, Daële V (2022) Diurnal variation and potential sources of indoor formaldehyde at elementary school, high school and university in the Centre Val de Loire region of France. Science of The Total Environment 811:152271.
4. Peng W-X, Yue X, Chen H, Ma N L, Quan Z, Yu Q, Wei Z, Guan R, Lam S S, Rinklebe J, Zhang D, Zhang B, Bolan N, Kirkham M B, Sonne C (2022) A review of plants formaldehyde metabolism: Implications for hazardous emissions and phytoremediation. Journal of Hazardous Materials 436:129304.
5. Wojnowski W, Yang A, Mikoviny T, Wisthaler A, Thunshelle K (2024) Exposure to cooking emitted volatile organic compounds with recirculating and extracting ventilation solutions. Building and Environment 261:111743.
6. Nielsen G D, Larsen S T, Wolkoff P (2017) Re-evaluation of the WHO (2010) formaldehyde indoor air quality guideline for cancer risk assessment. Archives of Toxicology 91:35-61.
7. Hua Y, Vikrant K, Kim K-H, Heynderickx P M, Boukhvalov D W (2025) Room temperature thermocatalytic removal of formaldehyde in air using a copper manganite spinel-supported palladium catalyst with ultralow noble metal content. Separation and Purification Technology 354:128863.
8. Qian R, Zong H, Schneider J, Zhou G, Zhao T, Li Y, Yang J, Bahnemann D W, Pan J H (2019) Charge carrier trapping, recombination and transfer during TiO_2 photocatalysis: An overview. Catalysis Today 335:78-90.
9. Lim D-H, Bathla A, Anwer H, Younis S A, Boukhvalov D W, Kim K-H (2024) The effects of nitrogen-doping on photocatalytic mineralization of TiO_2 nanocatalyst against formaldehyde in ambient air. Chinese Journal of Catalysis 59:303-323.
10. Maitlo H A, Anand B, Kim K-H (2024) TiO_2-based photocatalytic generation of hydrogen from water and wastewater. Applied Energy 361:122932.
11. Maitlo H A, Hu Z, Ali I, Maitlo G, Lim D-H, Afridi M N, Zhou M (2024) Recent development in advanced photocatalytic materials for oxidative removal of bisphenol. Journal of Cleaner Production 434:140291.
12. Ali Maitlo H, Younis S A, Kim K-H (2025) Understanding oxidation potential and degradation mechanism of acid-treated TiO_2 coupled g-C_3N_4 S-scheme heterojunction photocatalyst for the removal of gaseous formaldehyde. Separation and Purification Technology 356:129862.
13. Zhang Y, Wang D, Luo X, Chen Y, Lei K, Mao L, Duan Y, Zeng X, Wan G, Zhao Q, Sun Y (2024) Facile construction of Bi_2WO_6/TiO_2 microspheres heterojunction for boosting photocatalytic degradation of organic dyes. Inorganic Chemistry Communications 165:112543.
14. Rong A, Shi H, Zhao Q, Zhu H, Wang H, Yan G (2024) Boosted photocatalytic performance of hydrogen evolution and formaldehyde degradation with a S-scheme $PMo_{12}/MgIn_2S_4$ heterojunction. Separation and Purification Technology 348:127782.
15. Wang J, Xu X, Shen Y (2022) Constructing S-scheme CeO_2/CN heterojunction for high efficiency light-induced photothermal synergistic catalytic degradation of gaseous formaldehyde under visible light irradiation. Journal of Environmental Chemical Engineering 10:107436.
16.Kovalevskiy N, Cherepanova S, Gerasimov E, Lyulyukin M, Solovyeva M, Prosvirin I, Kozlov D, Selishchev D (2022). Enhanced Photocatalytic Activity and Stability of Bi_2WO_6–TiO_2-N Nanocomposites in the Oxidation of Volatile Pollutants. Nanomaterials 12:359.
17. Collado L, Gomez-Mendoza M, García-Tecedor M, Oropeza F E, Reynal A, Durrant J R, Serrano D P, de la Peña O'Shea V A (2023) Towards the improvement of methane production in CO_2 photoreduction using Bi_2WO_6/TiO_2 heterostructures. Applied Catalysis B: Environmental 324:122206.
18. Yang H, Zhao S, Zhuang X, Asuha S (2022) Hydrothermal synthesis of Bi_2WO_6/mesoporous TiO_2 nanocomposites and their adsorptive properties. Journal of Nanoparticle Research 24:159.
19. Zhu Z, Wan S, Zhao Y, Qin Y, Ge X, Zhong Q, Bu Y (2021) Recent progress in Bi_2WO_6-Based photocatalysts for clean energy and environmental remediation: Competitiveness, challenges, and future perspectives. Nano Select 2:187-215.
20. Shang M, Wang W, Zhang L, Sun S, Wang L, Zhou L (2009) 3D Bi_2WO_6/TiO_2 Hierarchical Heterostructure: Controllable Synthesis and Enhanced Visible Photocatalytic Degradation Performances. The Journal of Physical Chemistry C 113:14727-14731.
21. Murcia López S, Hidalgo M C, Navío J A, Colón G (2011) Novel Bi_2WO_6–TiO_2 heterostructures for

Rhodamine B degradation under sunlike irradiation. Journal of Hazardous Materials 185:1425-1434.
22. Xu J, Wang W, Sun S, Wang L (2012) Enhancing visible-light-induced photocatalytic activity by coupling with wide-band-gap semiconductor: A case study on Bi_2WO_6/TiO_2. Applied Catalysis B: Environmental 111-112:126-132.
23. Yao L, Wang W, Liang Y, Fu J, Shi H (2019) Plasmon-enhanced visible light photoelectrochemical and photocatalytic activity of gold nanoparticle-decorated hierarchical TiO_2/Bi_2WO_6 nanorod arrays. Applied Surface Science 469:829-840.
24. Chang H, Jiang M, Zhu Q, Liu A, Wu Y, Li C, Ji X, Gong L, Li S, Chen Z, Kong L, Han L (2022) A novel photoelectrochemical immunosensor based on $TiO_2@Bi_2WO_6$ hollow microspheres and Ag_2S for sensitive detection of SARS-COV-2 nucleocapsid protein. Microchemical Journal 182:107866.
25. Ahmadi M, Alavi S M, Larimi A (2023) UV–vis light responsive Bi_2WO_6 nanosheet/TiO_2 nanobelt heterojunction photo-catalyst for CO_2 reduction. Catalysis Communications 179:106681.
26. Jia Y, Zhan S, Ma S, Zhou Q (2016) Fabrication of TiO_2–Bi_2WO_6 Binanosheet for Enhanced Solar Photocatalytic Disinfection of E. coli: Insights on the Mechanism. ACS Applied Materials & Interfaces 8:6841-6851.
27. Chai Y, Zhou F, Zhu Z (2019) High-efficiency and environment-friendly sterilization PEVE coatings modified with Bi_2WO_6/TiO_2 composites. Chemical Physics Letters 715:173-180.
28. Mamaghani A H, Haghighat F, Lee C-S (2017) Photocatalytic oxidation technology for indoor environment air purification: The state-of-the-art. Applied Catalysis B: Environmental 203:247-269.
29. Li Y-W, Ma W-L (2021) Photocatalytic oxidation technology for indoor air pollutants elimination: A review. Chemosphere 280:130667.
30. Zhang Y, Fei L, Jiang X, Pan C, Wang Y (2011) Engineering Nanostructured Toward Effective Utilization of Natural Light in Photocatalysis. Journal of the American Ceramic Society 94:4157-4161.
31. Du Z, Cheng C, Tan L, Lan J, Jiang S, Zhao L, Guo R (2018) Enhanced photocatalytic activity of Bi_2WO_6/TiO_2 composite coated polyester fabric under visible light irradiation. Applied Surface Science 435:626-634.
32. Hao X, Zhou J, Cui Z, Wang Y, Wang Y, Zou Z (2018) Zn-vacancy mediated electron-hole separation in ZnS/g-C_3N_4 heterojunction for efficient visible-light photocatalytic hydrogen production. Applied Catalysis B: Environmental 229:41-51.
33. Zhang L, Meng G, Liu B, Ge X (2022) Heterogeneous photocatalytic ozonation of sulfamethoxazole by Z-scheme Bi_2WO_6/TiO_2 heterojunction: Performance, mechanism and degradation pathway. Journal of Molecular Liquids 360:119427.
34.D'Amato C A, Giovannetti R, Zannotti M, Rommozzi E, Minicucci M, Gunnella R, Di Cicco A (2018) Band Gap Implications on Nano-TiO_2 Surface Modification with Ascorbic Acid for Visible Light-Active Polypropylene Coated Photocatalyst. Nanomaterials 8:599.
35. Zhou Y, Zhang Y, Lin M, Long J, Zhang Z, Lin H, Wu J C S, Wang X (2015) Monolayered Bi_2WO_6 nanosheets mimicking heterojunction interface with open surfaces for photocatalysis. Nature Communications 6:8340.
36. Chen L, Ren J-T, Yuan Z-Y (2023) Enabling Internal Electric Fields to Enhance Energy and Environmental Catalysis. Advanced Energy Materials 13:2203720.
37. Khatun S, Pal S, Roy P (2024) Surface oxygen vacancy engineering of Cr-doped $FeNi_3/NiFe_2O_4$ Mott-Schottky heterojunction as efficient electrocatalyst for high current density water oxidation. Journal of Alloys and Compounds 977:173393.
38.Lasia A, 2014. Semiconductors and Mott-Schottky Plots. in: Lasia, A. (Ed.). Electrochemical Impedance Spectroscopy and its Applications. Springer New York, New York, NY, pp.251-255.
39. Bhat S S M, S G K (2025) Recent advances in interface engineering of bismuth-based materials for photocatalytic CO_2 reduction. RSC Applied Interfaces 2:1507-1526.
40. Li B, Liu X, Zhu H, Guan H, Guo R (2024) A Review on Bi_2WO_6-Based Materials for Photocatalytic CO_2 Reduction. Small 20:2406074.
41. Wen S, Zhang W, Yang J, Zhou Z, Xiang Q, Dong H (2024) Ternary Bi_2WO_6/TiO_2–Pt Heterojunction Sonosensitizers for Boosting Sonodynamic Therapy. ACS Nano 18:23672-23683.
42. Parrino F, Livraghi S, Giamello E, Ceccato R, Palmisano L (2020) Role of Hydroxyl, Superoxide, and Nitrate Radicals on the Fate of Bromide Ions in Photocatalytic TiO_2 Suspensions. ACS Catalysis 10:7922-7931.
43. Leng W, Zhang Z, Zhang J, Cao C (2005) Investigation of the Kinetics of a TiO_2 Photoelectrocatalytic Reaction Involving Charge Transfer and Recombination through Surface States by Electrochemical Impedance Spectroscopy. The Journal of Physical Chemistry B 109:15008-15023.

44. Meng S, Zhang J, Chen S, Zhang S, Huang W (2019) Perspective on construction of heterojunction photocatalysts and the complete utilization of photogenerated charge carriers. Applied Surface Science 476:982-992.
45. Jing L, Qu Y, Wang B, Li S, Jiang B, Yang L, Fu W, Fu H, Sun J (2006) Review of photoluminescence performance of nano-sized semiconductor materials and its relationships with photocatalytic activity. Solar Energy Materials and Solar Cells 90:1773-1787.
46. Lu Y, Younis S A, Chen C, Lu Z, Kim K-H (2025) Unveiling an inverted S-scheme pathway in nickel oxide/titanium dioxide for enhanced photocatalytic oxidation of gaseous formaldehyde. Composites Part B: Engineering 306:112834.
47. Masresha G, Jabasingh S A, Kebede S, Doo-Arhin D, Assefa M (2023) A review of prospects and challenges of photocatalytic decomposition of volatile organic compounds (VOCs) under humid environment. The Canadian Journal of Chemical Engineering 101:6905-6918.
48. Sun S, Vikrant K, Verma S, Boukhvalov D W, Kim K-H (2024) Diaminopropane-appended activated carbons for the adsorptive removal of gaseous formaldehyde using a portable indoor air purification unit. Journal of Colloid and Interface Science 653:992-1005.
49. Jeong M-G, Park E-J, Seo H-O, Kim K-D, Kim Y-D, Lim D-C (2013) Humidity effect on photocatalytic activity of TiO_2 and regeneration of deactivated photocatalysts. Applied Surface Science 271:164-170.
50. Malayeri M, Haghighat F, Lee C-S (2019) Modeling of volatile organic compounds degradation by photocatalytic oxidation reactor in indoor air: A review. Building and Environment 154:309-323.
51.Jiang X, Xu W, Yu L, 2019. Photocatalytic Decomposition of Gaseous HCHO over Ag Modified TiO_2 Nanosheets at Ambient Temperature. Nanomaterials 9:338.
52. Yu J, Yu H, Cheng B, Zhou M, Zhao X (2006) Enhanced photocatalytic activity of TiO_2 powder (P25) by hydrothermal treatment. Journal of Molecular Catalysis A: Chemical 253:112-118.
53. Nagyné-Kovács T, Shahnazarova G, Lukács I E, Szabó A, Hernadi K, Igricz T, László K, Szilágyi I M, Pokol G (2019) Effect of pH in the Hydrothermal Preparation of Bi_2WO_6 Nanostructures. Materials 12:1728.
54. Li N, Huang B, Dong X, Luo J, Wang Y, Wang H, Miao D, Pan Y, Jiao F, Xiao J, Qu Z (2022) Bifunctional zeolites-silver catalyst enabled tandem oxidation of formaldehyde at low temperatures. Nature Communications 13:2209.
55. Hao B, Ahmadi Y, Zhang T, Chen C, Lu Z, Ma H, Kim K-H (2025) Ultrathin K-doped g-C_3N_4/BiOBr heterojunctions with S-scheme charge transfer for efficient photodegradation of tetracycline. Journal of Environmental Management 391:126677.
56. Olawole O C, De D K, Olawole O F, Lamba R, Joel E S, Oyedepo S O, Ajayi A A, Adegbite O A, Ezema F I, Naghdi S, Olawole T D, Obembe O O, Oguniran K O (2022) Progress in the experimental and computational methods of work function evaluation of materials: A review. Heliyon 8:e11030.
57. Lejaeghere K, Van Speybroeck V, Van Oost G, Cottenier S (2014) Error Estimates for Solid-State Density-Functional Theory Predictions: An Overview by Means of the Ground-State Elemental Crystals. Critical Reviews in Solid State and Materials Sciences 39:1-24.
58. Tasbihi M, Bendyna J K, Notten P H L, Hintzen H T (2015) A Short Review on Photocatalytic Degradation of Formaldehyde. Journal of Nanoscience and Nanotechnology 15:6386-6396.
59. Wang C, Ge B, Jiang P, Xu F, Cheng C, Huang C (2025) Photocatalytic apparent quantum yield exceeding 100% achieved by photo–thermal synergistic impact ionization. Applied Surface Science 690:162638.
60. Chen M, Wang H, Chen X, Wang F, Qin X, Zhang C, He H (2020) High-performance of Cu-TiO_2 for photocatalytic oxidation of formaldehyde under visible light and the mechanism study. Chemical Engineering Journal 390:124481.
61. Ma L, Huang C, Li X, An X, Li J, Zou L, Zhu X, Yuan C, Dai X, Zhou Y, Zhu X, Tian C (2025) In situ synthesis of mesoporous TiO_2 doped with bismuth single atoms for tunable photocatalytic degradation of formaldehyde. Separation and Purification Technology 354:128635.
62. Jiang Z, Wang T, Wang J, Yu T, Kong C, Yang Z, Zhu H (2025) Oxygen vacancy-rich $BiVO_4$ modified with mesoporous MIL-88A(Fe) Z-scheme heterojunction for enhanced photocatalytic formaldehyde degradation. Separation and Purification Technology 353:128581.
63. He X, Vikrant K, Boukhvalov D W, Kim K-H (2025) Synthesis, performance, and reaction mechanisms of titanium dioxide-silicon carbide as a step-scheme heterojunction photocatalyst against formaldehyde in air. Chemical Engineering Journal 519:164114.
64. Qiu S, Wang W, Yu J, Tian X, Li X, Deng Z, Lin F, Zhang Y (2022) Enhanced photocatalytic degradation efficiency of formaldehyde by in-situ fabricated TiO_2/C/$CaCO_3$ heterojunction photocatalyst from mussel shell extract. Journal of Solid State Chemistry 311:123110.

915

916 **Table 1.** Physical characteristics of TB-x series catalysts along with the reference materials
917 (Bi_2WO_6 and TiO_2).

Order	Material	BET surface area	Total pore volume	Average pore diameter
		$m^2\ g^{-1}$	$cm^3\ g^{-1}$	nm
1	Bi_2WO_6	72.78	0.17	5.22
2	TiO_2	49.30	0.07	4.7
3	TB-2	46.03	0.09	4.68
4	TB-5	45.97	0.08	4.39
5	TB-10	52.55	0.11	5.19

918

Table 2. Comparison of FA photocatalytic oxidation performance of TB-x series catalysts along with the Bi_2WO_6 and TiO_2 under varied operating parameters within 13 minutes

Order	Material	Light condition	X_{FA} (%)	RH (%)	Mass g	FA conc. ppm	Flow rate L min^{-1}	O_2 conc. (%)	Synthesis time (hour)	CADR L min^{-1}	SCADR L min^{-1} g^{-1}	r_{10} mmol g^{-1} h^{-1}	r_{max} mmol g^{-1} h^{-1}	AQY %	MAQY molecules $photon^{-1}$ g^{-1}
(a) Photocatalyst															
1	Bi_2WO_6		56.6		0.096					3.11	32.25	0.58	0.13	1.17E-01	1.21E-02
2	TiO_2		98.7		0.100					5.73	59.51	1.11	0.22	2.04E-01	2.04E-02
3	TB-2	Light on	100		0.094					6.50	69.17	0.95	0.28	2.44E-01	2.60E-02
4	TB-5		100		0.084					10.37	123.80	1.72	0.35	2.68E-01	3.20E-02
5	TB-10		100	0	0.097	5	160	21	15	9.33	96.66	1.35	0.30	2.68E-01	2.78E-02
6	Bi_2WO_6		39.5		0.096					2.01	22.34	0.41	0.09	-	-
7	TiO_2		39		0.100					1.98	20.56	0.51	0.09	-	-
8	TB-2	Light off	29.1		0.094					1.04	11.07	0.16	0.07	-	-
9	TB-5		27.8		0.084					1.40	14.85	0.28	0.07	-	-
10	TB-10		34		0.097					1.75	18.12	0.38	0.08	-	-
(b) RH															
11			100	0						10.37	123.80	1.77	0.35	2.68E-01	3.20E-02
12	TB-5	Light on	100	20	0.084	5	160	21	15	6.15	73.35	1.06	0.29	2.24E-01	2.67E-02
13			92.3	50						3.38	40.36	0.63	0.25	1.91E-01	2.27E-02
14			74.8	80						2.33	27.76	0.53	0.20	1.54E-01	1.84E-02
(c) Mass loading															
15			36.47		0.022					0.71	32.40	0.71	0.10	7.54E-02	3.44E-02
16	TB-5	Light on	100	0	0.046	5	160	21	15	5.31	115.24	1.64	0.29	2.24E-01	4.85E-02
17			100		0.084					10.37	123.80	1.77	0.35	2.68E-01	3.20E-02
(d) FA conc.															
18			100			1				21.09	251.65	0.41	0.23	1.79E-01	2.13E-02
19	TB-5	Light on	100	0	0.084	3	160	21	15	11.94	142.51	1.12	0.37	2.68E-01	3.20E-02
20			100			5				10.37	123.80	1.77	0.35	2.68E-01	3.20E-02
(e) Flow rate															
21			100				100			7.04	84.01	1.42	0.29	2.24E-01	2.67E-02
22	TB-5	Light on	100	0	0.084	5	130	21	15	7.42	88.56	1.37	0.32	2.44E-01	2.91E-02
23			100				160			10.37	123.80	1.77	0.35	2.68E-01	3.20E-02
(f) O_2 conc.															
24			54.44					0		2.44	29.14	0.95	0.15	1.12E-01	1.34E-02
25	TB-5	Light on	81.37	0	0.084	5	160	10	15	3.30	39.43	1.14	0.22	1.68E-01	2.01E-02
26			100.00					21		10.37	123.80	1.77	0.35	2.68E-01	3.20E-02
(g) Different hydrothermal time															
27			99.7		0.099				6	11.05	110.74	1.55	0.23	2.06E-01	2.08E-02
28	TB-5	Light on	100	0	0.084	5	160	21	15	10.37	123.80	1.77	0.35	2.68E-01	3.20E-02
29			98.3		0.073				48	7.79	107.34	1.75	0.31	2.03E-01	2.80E-02
(h) Reusability															
30			100							10.63	126.85	1.80	0.35	2.68E-01	3.20E-02
31			100							10.51	125.45	1.72	0.39	2.98E-01	3.56E-02
32	TB-5	Light on	100	0	0.084	5	160	21	15	9.99	119.26	1.09	0.35	2.68E-01	3.20E-02
33			100							10.31	123.05	1.52	0.39	2.98E-01	3.56E-02
34			100							10.21	121.91	1.62	0.27	2.06E-01	2.46E-02

Table 3. The removal performance of FA between different photocatalytic systems (TB-5 vs. ones reported previously)

Order	Catalyst	Light source	m_{cat} (mg)	FA concentration (ppm)	Irradiation time (h)	X_{FA} (%)	r_{max} (mmol mg^{-1} h^{-1})	AQY (%)	MAQY (molecules $photon^{-1}$ g^{-1})	CADR (L min^{-1})	Reference
1	Cu-TiO_2	500 W Xe lamp	100	250	2.33	100	0.07	9.70E-04	9.70E-03	-	[60]
2	NiO-TiO_2	1 W UV lamp	81.3	1	0.1	100	0.085	6.34E-02	7.79E-03	10.35	[46]
				5	0.17	100	0.183	1.36E-01	1.62E-02	6.55	
3	Bi-TiO_2	300 W Xe lamp	30	40	0.25	93	0.02	1.60E-05	5.35E-06	0.02	[61]
4	$BiVO_4$ OVs-MIL-88A(Fe)	30 W Xe lamp	200	50	2	91.8	0.03	1.47E-03	7.36E-05	0.12	[62]
5	N-TiO_2	1W UV lamp	59.9	5	0.08	93	0.65	3.54E-01	5.90E-02	9.45	[9]
6	TiO_2-SiC	1W UV lamp	100	1	0.03	100	0.21	1.90E-01	1.90E-02	18.53	[63]
			100	5	0.17	90	0.2	1.75E-01	1.75E-02	8.45	
7	TiO_2/C/$CaCO_3$	300 W Xe lamp	200	358	1.33	100	0.05	2.89E-04	1.45E-05	0.37	[64]
8	TB-5	1 W UV lamp	83.8	1	0.05	100	0.23	1.79E-01	2.13E-02	21.09	This study
			83.8	5	0.17	100	0.35	2.68E-01	3.20E-02	10.37	

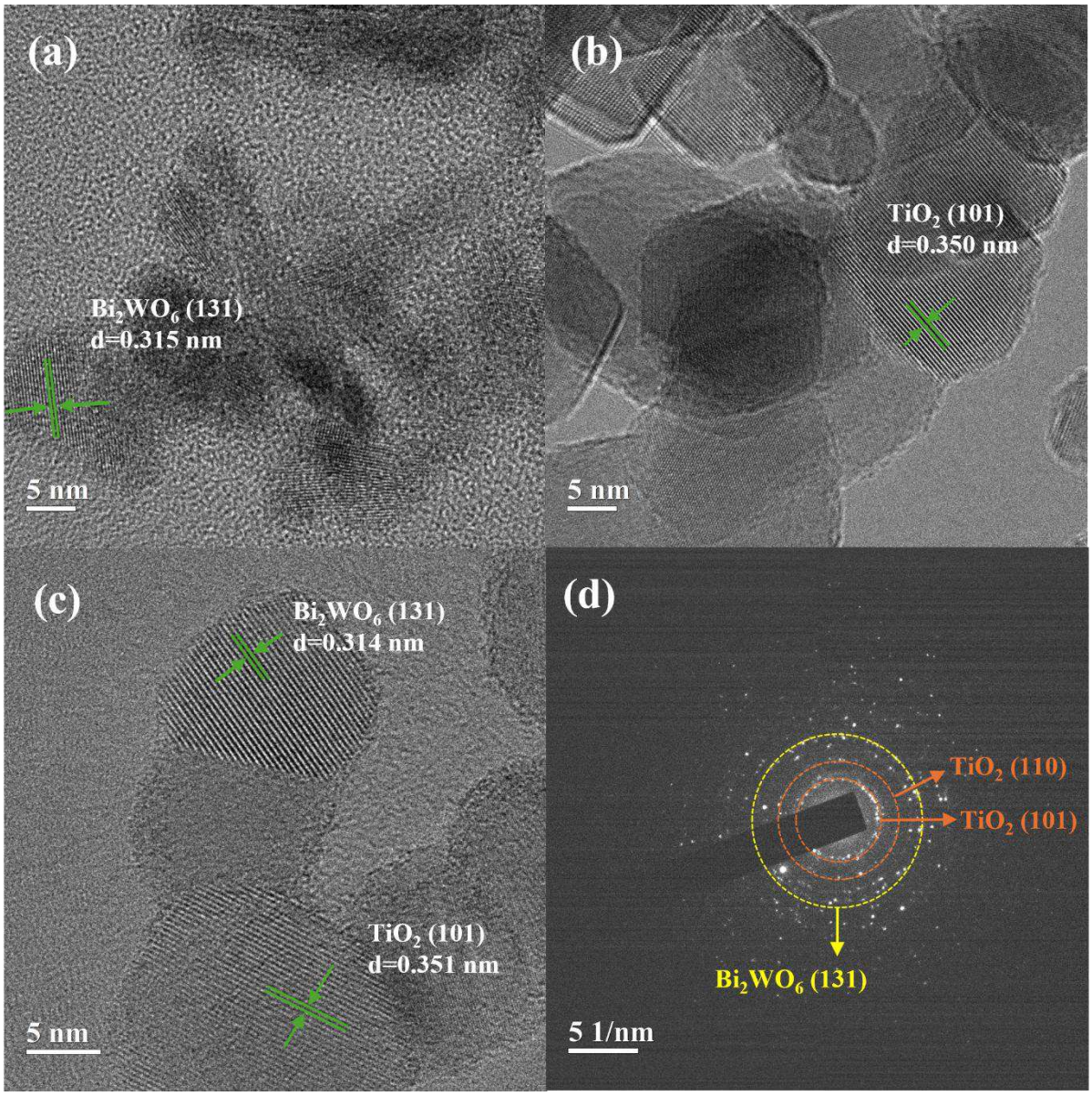
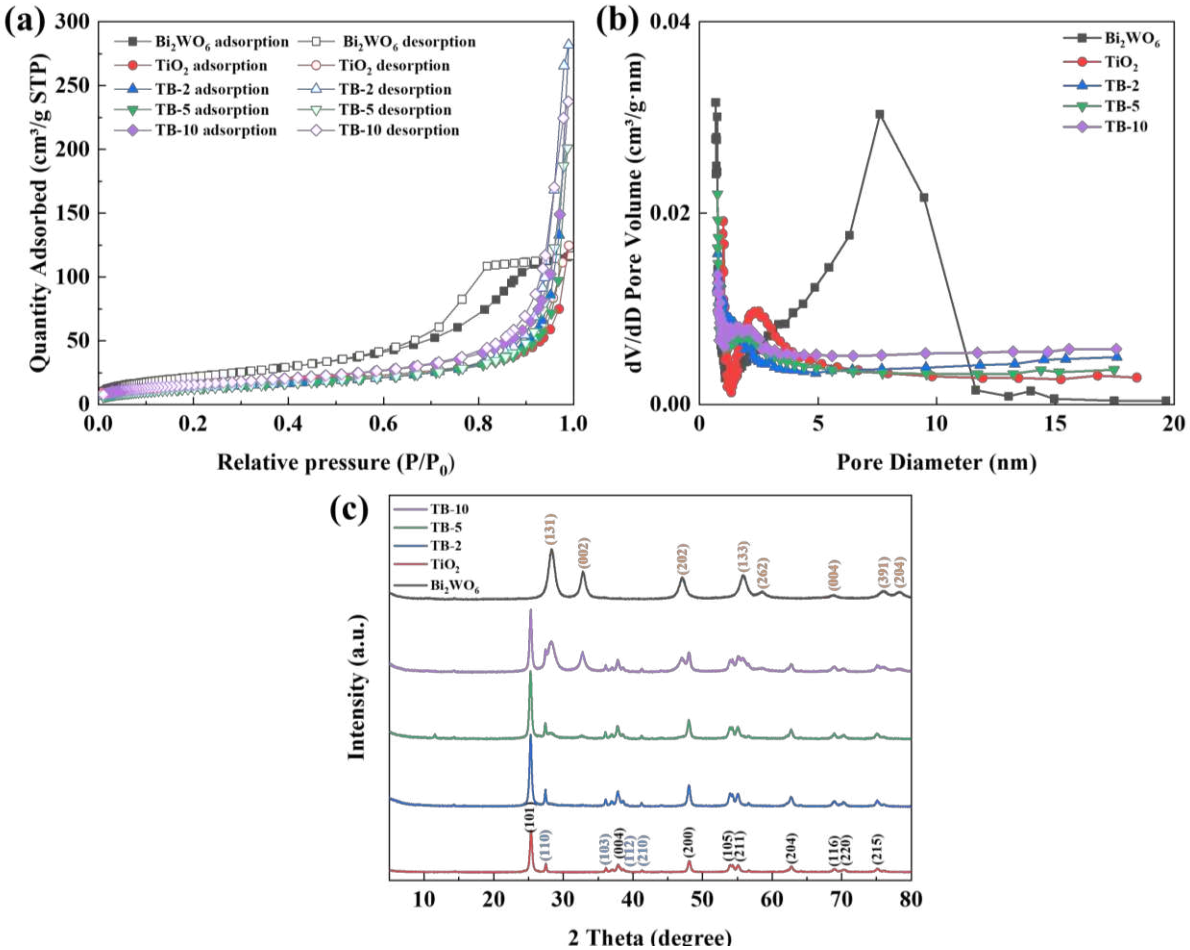


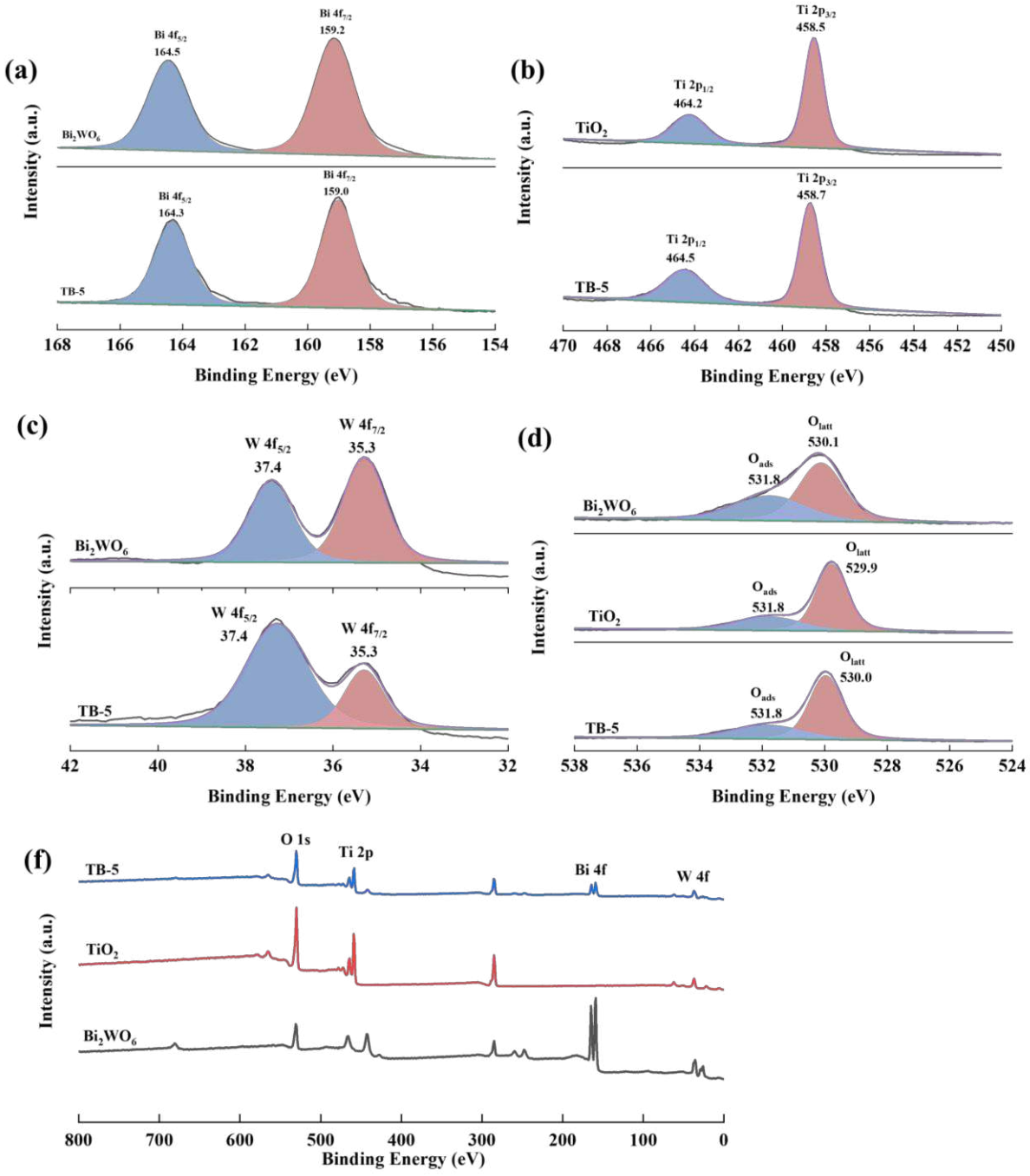
Figure 1. TEM micrographs of the tested photocatalysts: (a) Bi_2WO_6, (b) TiO_2, (c) TB-5, and (d) SAED pattern of TB-5.



927

928 **Figure 2.** Surface properties of TB-x series catalysts along with the reference materials
929 (Bi_2WO_6 and TiO_2) tested photocatalysts. (a) N_2 adsorption-desorption isotherms, (b) Pore size
930 distribution curves and (c) PXRD patterns.

931



932

933 **Figure 3.** XPS spectra of TB-5 along with the reference catalysts (Bi_2WO_6 and TiO_2): (a) Bi
934 4f, (b) Ti 2p, (c) W 4f, (d) O 1s, and (e) full XPS spectra

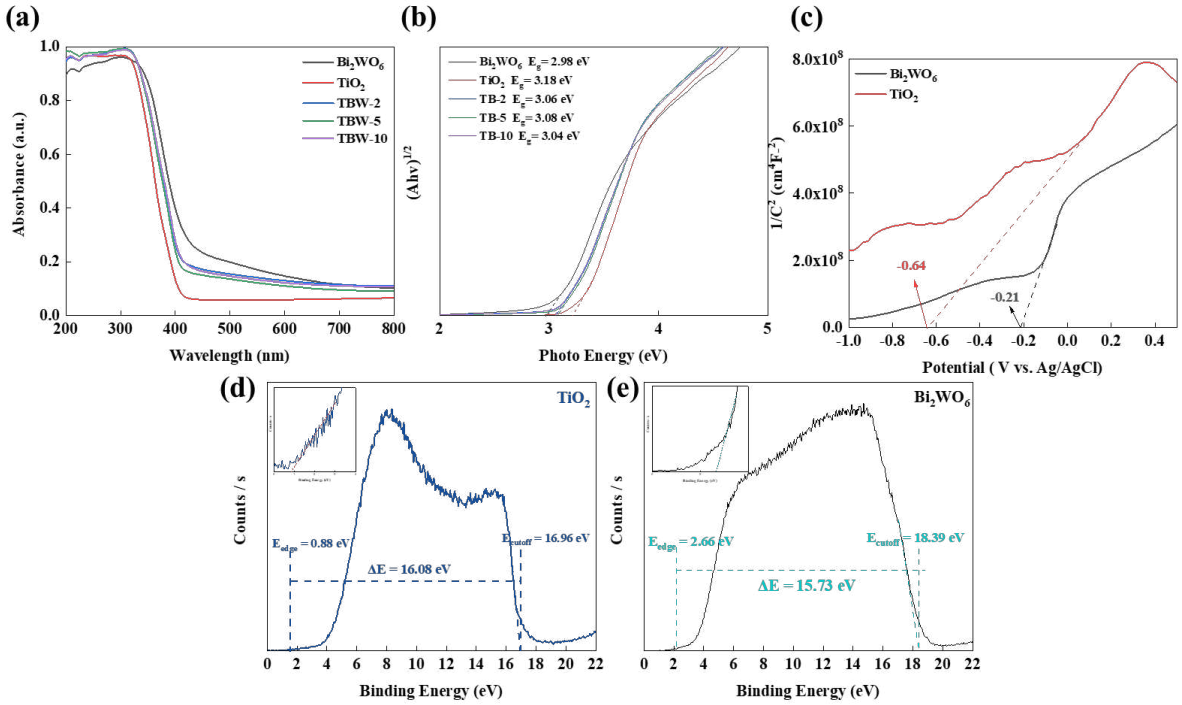


Figure 4. Optoelectronic characterization of TB-x series catalysts along with the reference materials (Bi_2WO_6 and TiO_2). (a) UV-vis spectra, (b) Tauc plots, (c) Mott-Schottky curves, (d) UPS spectra of TiO_2, and (e) UPS spectra of Bi_2WO_6.

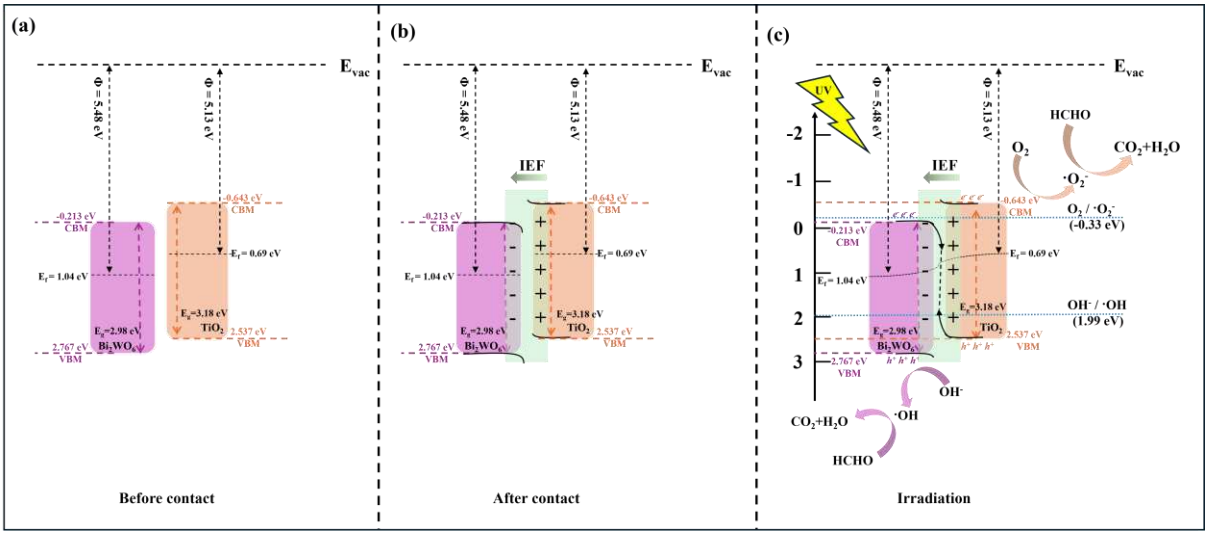
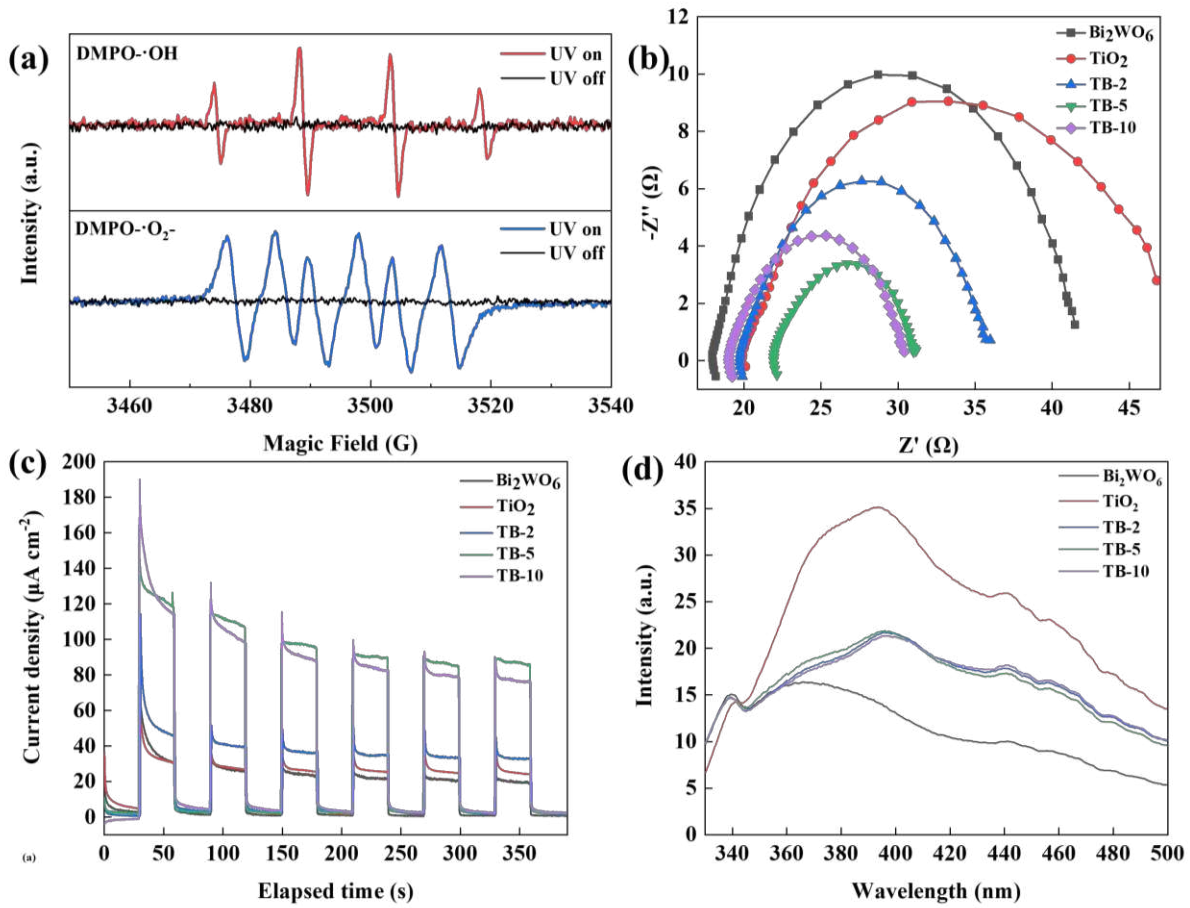


Figure 5. Plot of S-scheme heterojunction and the associated charge transfer mechanism between Bi_2WO_6 (as OP) and TiO_2 (as RP): (a) before contract and (b-c) after contact [under (b) dark and (c) light irradiation conditions].



945

946 **Figure 6.** Photoelectrochemical properties of the TB-x series catalysts along with the reference
947 materials (Bi_2WO_6 and TiO_2): (a) EPR spectra of TB-5, (b) EIS spectra, (c) Transient PC
948 response under UV on/off cycles, and (d) PL spectra.

949

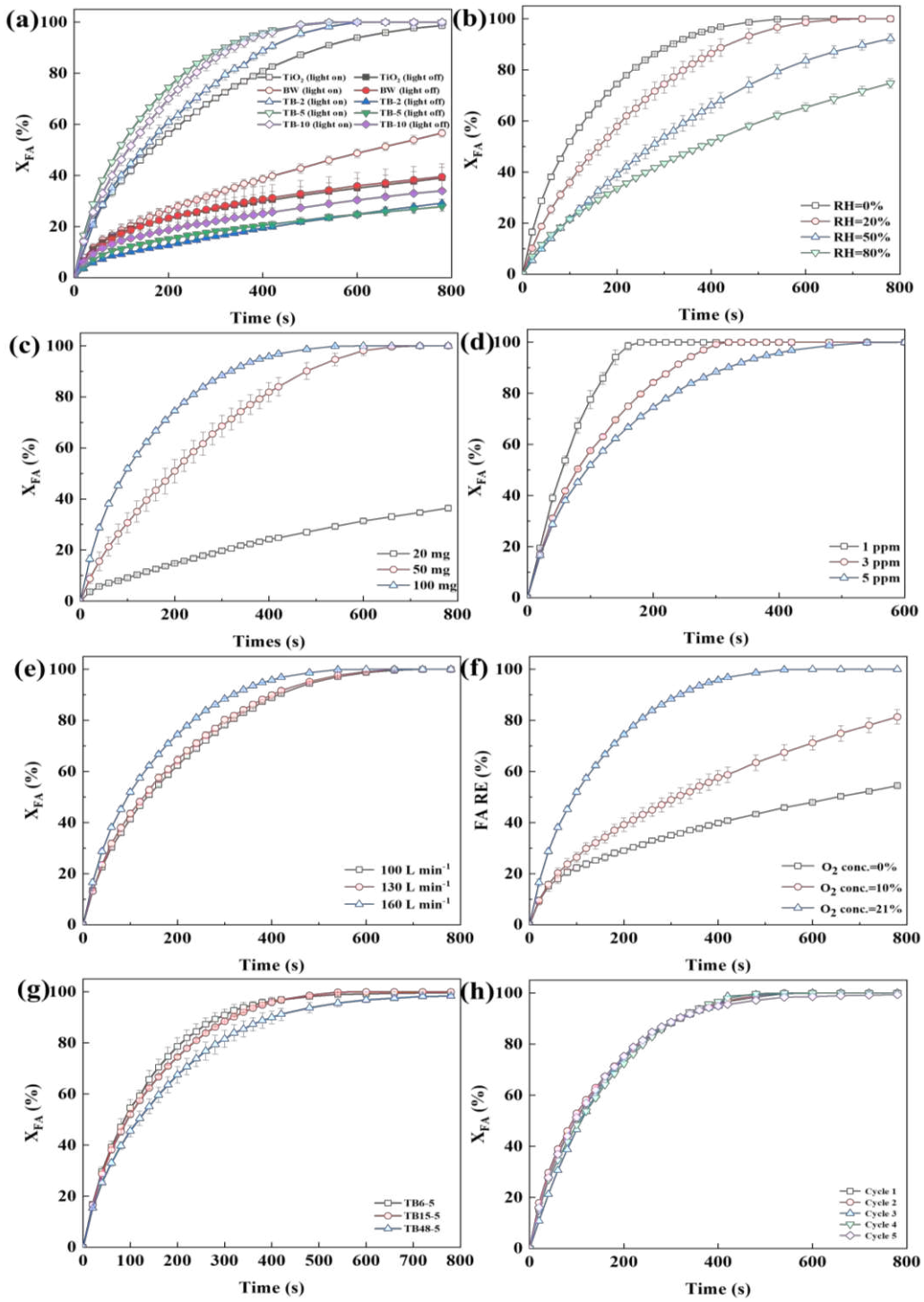
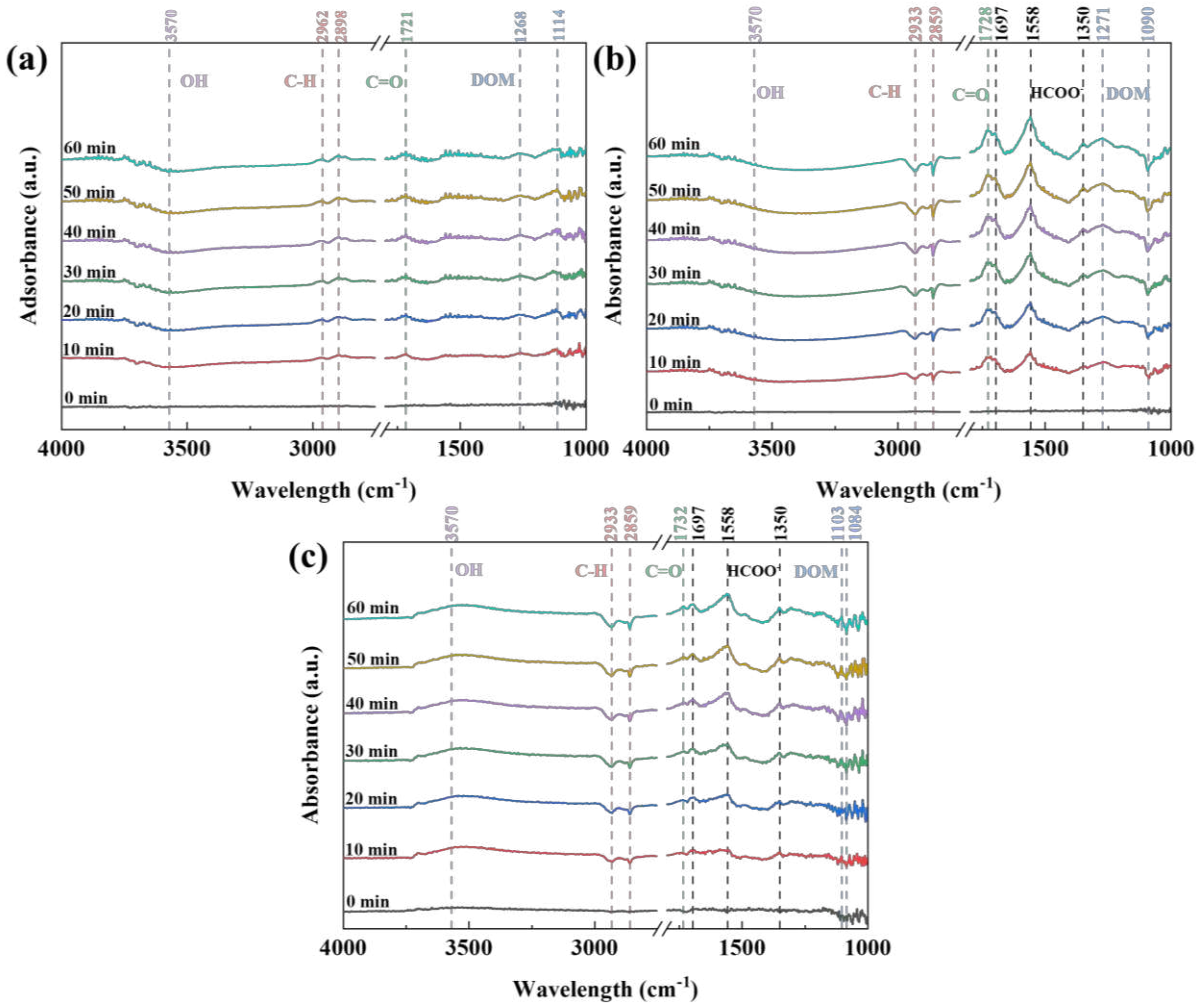


Figure 7. Comparison of PCO efficiency (X_{FA}) of TB-x photocatalysts (base conditions: FA= 5 ppm, m_{cat}=100 mg, flow rate=160 L min^{-1}, RH=0%, and O_2 concentration=21 vol.%): (a) all photocatalysts prepared in this study, (b-g) tests under control of each process variable ((b) RH, (c) m_{cat}, (d) FA concentration, (e) AP flow rate , (f) O_2 concentration, (g) hydrothermal duration (6, 15, and 48 h)), and (h) tests over five cycles



957

958 **Figure 8.** *In-situ* DRIFTS spectra of TB-5 under different reaction conditions: (a) FA + air +
959 UV off, (b) FA + air + UV on, and (c) FA + air + H_2O + UV on.

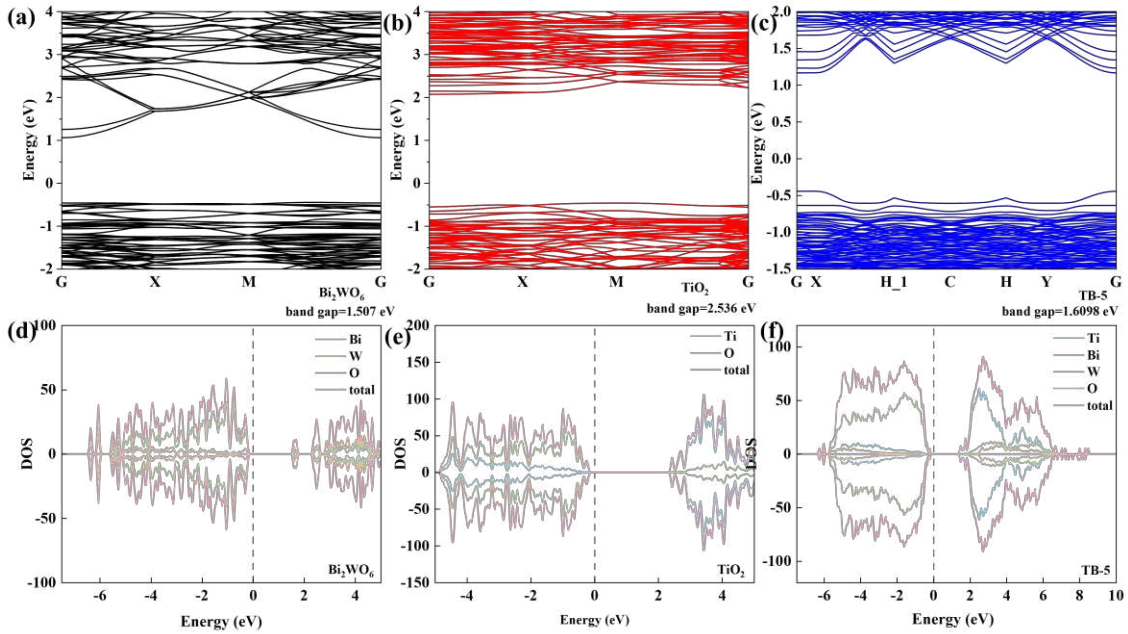
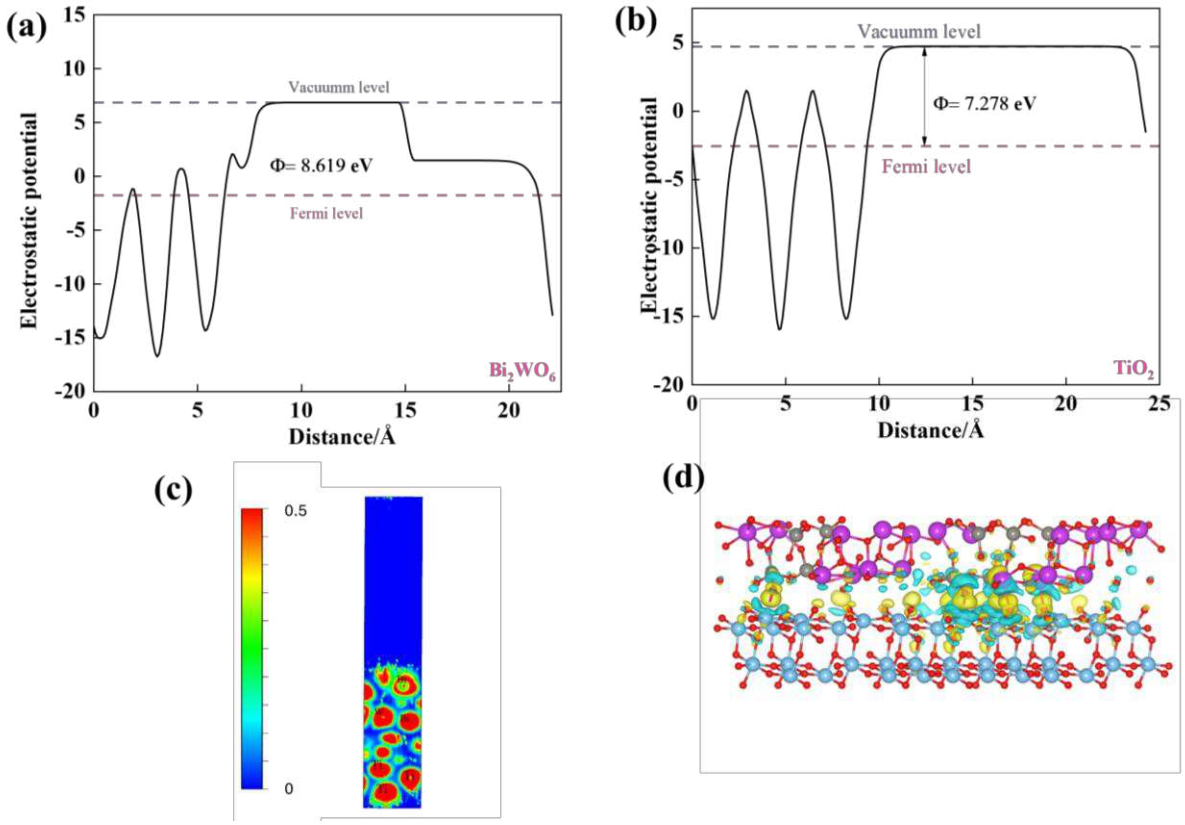


Figure 9. Calculated band structures: (a) Bi_2WO_6, (b) TiO_2 and (c) TB-5. DOS curves: (d) Bi_2WO_6, (e) TiO_2 and (f) TB-5.



963

964 **Figure 10.** Calculated work functions of (a) Bi_2WO_6 and (b) TiO_2. (c) Electron localization
965 function of TB-5 and (d) Charge density difference of TB-5 with an isosurface of 0.002 e/Bohr3.

Supplementary Information (SI)

Table S1. Detailed information of photocatalyst sample codes developed for the abatement of gaseous FA

		procedure mass (mg)			element component (mmol) [b]			molar ratio of Bi to Ti (%)
Order	Sample code	$Bi(NO3)_3{\cdot}5H_2O$	$Na_2WO_4{\cdot}2H_2O$	TiO_2	Bi (B)	WO_6 (W)	TiO_2 (T)	B/T
[A] Pristine material								
1	TiO_2	-	-	1,000.0	-	-	12.5	-
2	Bi_2WO_6	606.0	198.0	-	1.2	0.6	-	-
[B] heterojunction of TB-x [a]								
3	TB-2	121.2	39.6	1,000.0	0.2	0.1	12.5	2.00
4	TB-5	303.0	99.0	1,000.0	0.6	0.3	12.5	4.99
5	TB-10	606.0	198.0	1,000.0	1.2	0.6	12.5	9.98

a] Bi_2WO_6 composites with TiO_2 are named as TB-x, where x represents the percent value for the molar ratio of Bi to Ti

b] The molar weight of $Bi(NO_3)_3{\cdot}5H_2O$, $Na_2WO_4{\cdot}2H_2O$ and TiO_2 is 485.1 g mol^{-1}, 329.9 g mol^{-1} and 79.9 g mol^{-1}, respectively.

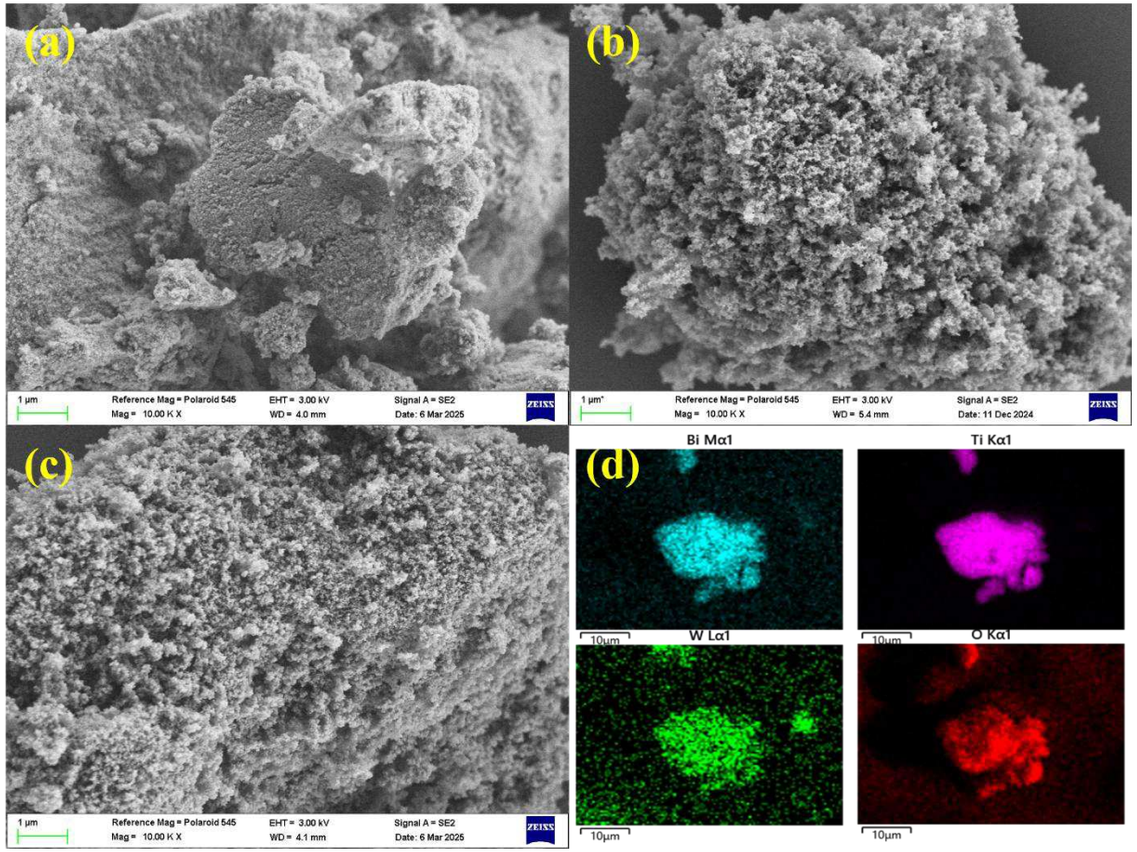


Figure S1. SEM images of the tested photocatalysts. (a) Bi_2WO_6, (b) TiO_2, (c) TB-5, and (d) EDS of TB-5.

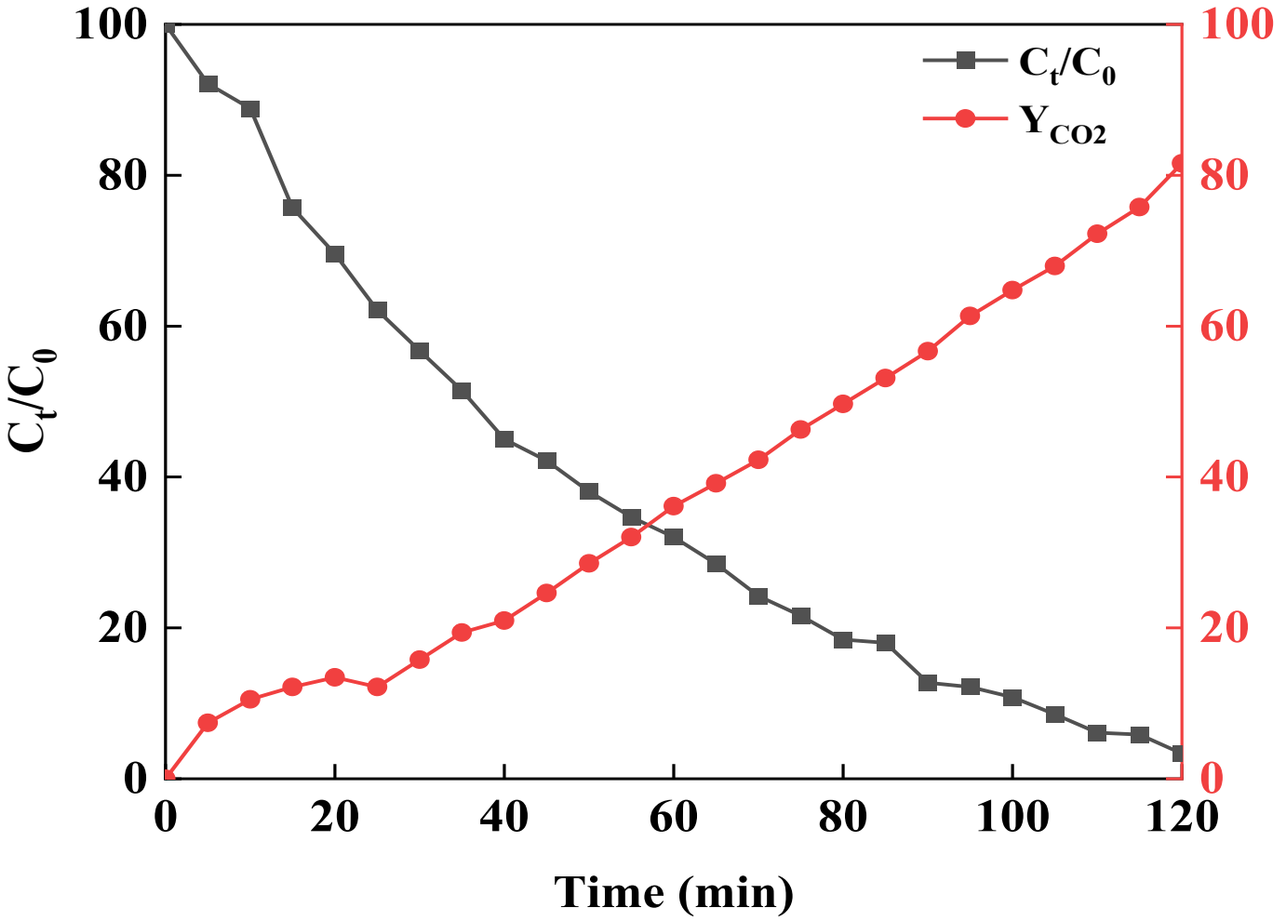


Figure S2. CO_2 yield (%) of TB-5 under 100 ppm of FA after 120 minutes